PHYSICAL SCIENCES

Positronium image of the human brain in vivo

Paweł Moskal[1,2]*, Jakub Baran[1,2], Steven Bass[1,2,3], Jarosław Choiński[4], Neha Chug[1,2], Catalina Curceanu[5], Eryk Czerwiński[1,2], Meysam Dadgar[1,2], Manish Das[1,2], Kamil Dulski[1,2], Kavya V. Eliyan[1,2], Katarzyna Fronczewska[6], Aleksander Gajos[1,2], Krzysztof Kacprzak[1,2], Marcin Kajetanowicz[1,2], Tevfik Kaplanoglu[1,2], Łukasz Kapłon[1,2], Konrad Klimaszewski[7], Małgorzata Kobylecka[6], Grzegorz Korcyl[1,2], Tomasz Kozik[1,2], Wojciech Krzemień[1,2,8], Karol Kubat[1,2], Deepak Kumar[1,2], Jolanta Kunikowska[6], Joanna Mączewska[6], Wojciech Migdał[1,2], Gabriel Moskal[2,9], Wiktor Mryka[1,2], Szymon Niedźwiecki[1,2], Szymon Parzych[1,2], Elena P. del Rio[1,2], Lech Raczyński[7], Sushil Sharma[1,2], Shivani Shivani[1,2], Roman Y. Shopa[7], Michał Silarski[1,2], Magdalena Skurzok[1,2], Faranak Tayefi[1,2], Keyvan T. Ardebili[1,2], Pooja Tanty[1,2], Wojciech Wiślicki[7], Leszek Królicki[6], Ewa Ł. Stępień[1,2]*

Positronium is abundantly produced within the molecular voids of a patient's body during positron emission tomography (PET). Its properties dynamically respond to the submolecular architecture of the tissue and the partial pressure of oxygen. Current PET systems record only two annihilation photons and cannot provide information about the positronium lifetime. This study presents the in vivo images of positronium lifetime in a human, for a patient with a glioblastoma brain tumor, by using the dedicated Jagiellonian PET system enabling simultaneous detection of annihilation photons and prompt gamma emitted by a radionuclide. The prompt gamma provides information on the time of positronium formation. The photons from positronium annihilation are used to reconstruct the place and time of its decay. In the presented case study, the determined positron and positronium lifetimes in glioblastoma cells are shorter than those in salivary glands and those in healthy brain tissues, indicating that positronium imaging could be used to diagnose disease in vivo.

INTRODUCTION

Positronium is abundantly produced in the patient's body during positron emission tomography (PET), and its properties (e.g., mean lifetime) are modified by the tissue submolecular environment (*1*, *2*). Therefore, positronium is considered a promising diagnostic indicator (*1*–*6*). The state-of-the-art PET scanners are limited to recording only two photons with an energy of 511 keV coming from electron-positron annihilation (*7*). They are therefore incapable of providing information about the positronium lifetime that requires the detection of an additional prompt gamma emitted from the radionuclide. The prompt gamma is needed to determine the time of positronium formation in the body, while annihilation photons signal the time of positronium decay (*8*). We have invented a method (*9*–*11*) and the Jagiellonian PET (J-PET) system (*8*) capable of imaging positronium lifetime (*9*–*11*) based on the registration of two photons from its annihilation and additional prompt gamma emitted by some of the isotopes [e.g., ^{68}Ga routinely used in PET diagnostics (*12*–*14*)]. The method was recently validated in ex vivo studies by reconstructing positronium images (*8*) and by observing differences in positronium mean lifetime between healthy and tumor tissues (*6*, *15*–*17*). Here, we demonstrate the in vivo positronium images of a human brain performed in clinics with a dedicated portable J-PET scanner (*18*) designed to enable a simultaneous registration of annihilation photons and prompt gamma originating from the radionuclide attached to the biomolecule. The advantage of the J-PET scanner, which makes this imaging possible, lies in its programmable electronics (*19*), triggerless data acquisition (DAQ) (*20*), and dedicated signal processing algorithms (*8*, *11*). These features are designed to enable the registration of three or even more photons simultaneously as well as the recording of photons with energies exceeding 511 keV. In a standard PET scan, biomolecules (tracers) labeled with a radionuclide that emits positrons are administered to the patient at picomolar concentrations. In the patient's body, positrons annihilate with electrons creating photons whose registration in the PET scanner enables imaging of the distribution of the labeled biomolecules in the body. Therefore, PET allows for the assessment of metabolic effects, transport activities, or receptor expression in vivo directly in the patient.

PET diagnostics has experienced continuous improvements in radiation detection (*21*) and radiopharmacy (*13*), from the first blurry brain tumor images achieved with two crystal scintillation detectors in 1953 (*22*), to the first application of fluorodeoxyglucose labeled with ^{18}F for brain metabolism imaging in 1979 (*23*) and the first scans with ^{68}Ga-labeled somatostatin receptors in 1999 (*12*), to the dynamic and simultaneous imaging of all patient tissues demonstrated in 2019 (*24*) with the total-body PET system constructed from 564,480 crystal scintillators (*25*).

However, after 70 years of development, the main principle of PET scanners of recording electron-positron annihilation into two photons and its applications based on localizing the accumulation of pharmaceuticals remained unchanged. For example, PET scans of

[1]Faculty of Physics, Astronomy and Applied Computer Science, Jagiellonian University, S. Łojasiewicza 11, 30-348 Krakow, Poland. [2]Centre for Theranostics, Jagiellonian University, Kopernika 40, 31-501 Krakow, Poland. [3]Kitzbühel Centre for Physics, Kitzbühel, Austria. [4]Heavy Ion Laboratory, University of Warsaw, Warsaw, Poland. [5]INFN, Laboratori Nazionali di Frascati, Via E. Fermi 40, 00044 Frascati, Italy. [6]Department of Nuclear Medicine, Medical University of Warsaw, Banacha 1a, 02-097 Warsaw, Poland. [7]Department of Complex Systems, National Centre for Nuclear Research, 05-400 Otwock-Świerk, Poland. [8]High Energy Department, National Centre for Nuclear Research, 05-400 Otwock-Świerk, Poland. [9]Department of Chemical Technology, Faculty of Chemistry of the Jagiellonian University, Gronostajowa 2, 30-387 Krakow, Poland.
*Corresponding author. Email: p.moskal@uj.edu.pl (P.M.); e.stepien@uj.edu.pl (E.Ł.S.)

the brain are mainly performed to locate lesions, including determining the location and size of brain tumors (*26*), to assess the measurement of cellular and tissue metabolism, to show blood flow, and to evaluate patients with seizure disorders (epilepsy) who do not respond to pharmacotherapy (*27*) and patients with memory impairment due to neurodegenerative diseases [Alzheimer's disease spectrum and Parkinson's disease (*28*)]. The detection of molecular alterations that is not currently achievable would be possible using positronium imaging, which would increase PET specificity for early recognition of these diseases before the functional changes occur (*1*). Methods capable of sensing and imaging the intramolecular environment, oxidation level, pH at the picomolar level, or electrolytes within the tissue and biological fluids are currently under development (*29*–*33*). For example, quantum chemical sensing with double-photon emission imaging (*29*, *30*) or perturbed angular correlation with radioisotope-chelated DOTA ^{111}In (*31*, *33*) has recently demonstrated sensitivity to pH changes in the range of the extracellular and intralysosomal environments.

This study focuses on the potential of intramolecular sensing using positron-electron annihilations via positronium. In the body, a positron emitted from the isotope attached to the biomolecule may annihilate with an electron either directly (~60% cases) or via the formation of positronium (~40% cases) (*2*). Positronium is a metastable atom made of an electron and a positron. It may be formed as a long-lived ($\tau_{oPs}^{vacuum} = 142$ ns) spin-one ortho-positronium (oPs) or as a short-lived ($\tau_{pPs}^{vacuum} = 125$ ps) spin-zero para-positronium (pPs). In vacuum, oPs decays into three photons (oPs → 3γ) and pPs into two photons (pPs → 2γ) (*2*). In the tissue (Fig. 1), the oPs lifetime ($\tau_{oPs}^{tissue} < \sim 4$ ns) is substantially shortened because, in addition to self-annihilation into three photons, the positron from oPs may pick off electrons from the surrounding molecular environment (pick-off process) and annihilate predominantly into two photons. The oPs lifetime may also be shortened by interacting with the dissolved oxygen molecules. oPs may react with a paramagnetic O_2 molecule via spin-exchange or oxidation processes (*4*, *34*). In the spin-exchange process, oPs is converted to pPs, which then rapidly decays into two photons (oPs + O_2 → pPs + O_2 → 2γ + O_2). Therefore, the smaller the inter- and intramolecular voids and the higher the oxygen concentration, the shorter the mean oPs lifetime also the smaller the rate ratio of oPs self-annihilations (oPs → 3γ) to oPs pick-off processes (oPs → 2γ). For example, oPs pick-off two-photon annihilations in the tissue with τ_{oPs}^{tissue} equal to 2 ns are about 70 times ($\tau_{oPs}^{vacuum}/\tau_{oPs}^{tissue} - 1$) more frequent than oPs self-annihilations into three photons. Figure 1 indicates possible decay mechanisms of positronium in the intramolecular spaces.

Current PET scanners use e^+e^- annihilation into two photons only, and they are insensitive to the positron annihilation mechanism that may deliver diagnostics information complementary to the presently available images of metabolic rate and receptor expression. For example, the early tissue alterations at the molecular level and the changes in the tissue oxidation could be sensed by knowing the ratio of 3γ to 2γ decay rate and the mean positronium lifetime (*1*, *2*, *4*). Therefore, positronium is considered as a promising biomarker of tissue pathology at the early stage of molecular alterations and as a biomarker of tissue oxidation (*2*–*4*).

Here, we demonstrate the in vivo images of positronium lifetime in the human brain. Figure 1 shows the photograph of the patient in the modular J-PET tomograph. The superimposed arrows indicate annihilation photons (blue dashed arrow) from the electron-positron annihilations, while the red solid arrow shows

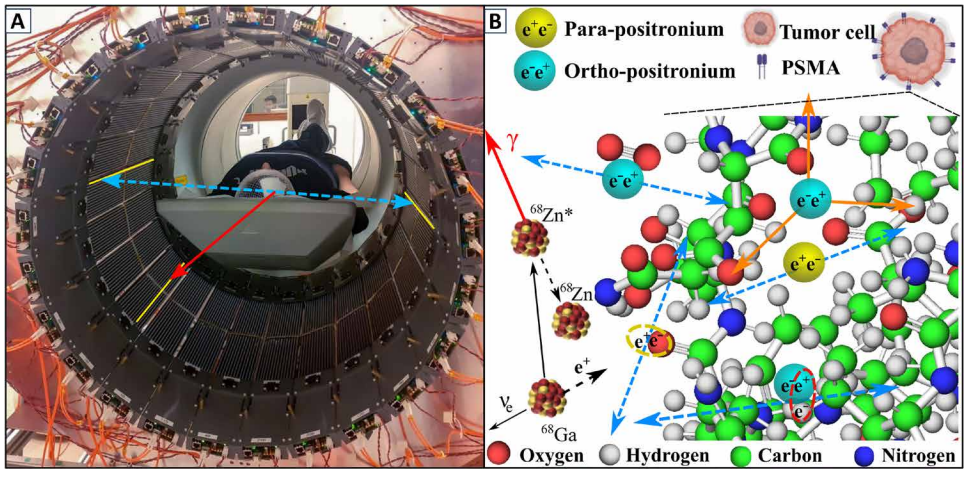

Fig. 1. Positronium imaging of a human brain. (**A**) Photograph of the patient in the modular J-PET tomograph. The patient diagnosed with brain glioma was intravenously and intratumorally administered with pharmaceuticals labeled with the ^{68}Ga radionuclide, which emits positrons and prompt gamma rays (the course of imaging is illustrated in Fig. 2). The superimposed arrows represent photons from electron-positron annihilation (blue dashed arrow) and prompt gamma from the deexcitation of the ^{68}Zn* radionuclide (red solid arrow). The plastic strips of the tomograph in which the gamma rays interacted have been highlighted in yellow. (**B**) Pictorial illustration of the ^{68}Ga isotope decay chain (^{68}Ga → ^{68}Zn* + e^+ + ν → ^{68}Zn + γ + e^+ + ν) and possible ways of positron and positronium annihilation within molecules on the example of the PSMA molecule overexpressed at the membrane of the microvascular endothelial cell (*38*). Positron (black dashed arrow) emitted by ^{68}Ga may annihilate directly (e^+e^- → photons) or via the formation of positronium (e^+e^- → Ps → photons) (*1*). Positronium (Ps) is formed as pPs (yellow) or oPs (blue). Blue dashed arrows indicate annihilations into two photons used for imaging. Main annihilation mechanisms mentioned in order of decreasing probabilities include (*2*): (i) direct annihilation (yellow ellipse), (ii) annihilation of a positron from oPs by picking off the electron from the atom (red ellipse), (iii) self-annihilation of pPs, (iv) conversion of oPs to pPs on the O_2 molecule proceeded by self-annihilation of pPs (oPs + O_2 → pPs + O_2 → 2γ + O_2), and (v) self-decay of oPs into three photons (orange arrows) inside the free space between atoms.

the prompt gamma from the ^{68}Zn isotope deexcitation. To determine the positronium lifetime in the patient, it is necessary to know the time of positronium formation and the time of its annihilation. The moment of annihilation is determined from the time when annihilation photons (blue dashed arrows in Fig. 1) interact in the detection system. The time of the positronium formation may be estimated if the radionuclide, in addition to the positron, also emits a prompt gamma (red solid arrow in Fig. 1). Registering the time when prompt gamma interacts in the detector system enables us to estimate the time of positronium formation (*10*, *11*).

In this study, the patient diagnosed with primary brain glioma was administered pharmaceuticals labeled with the ^{68}Ga radionuclide that, in 1.3% of positron emissions, also emits a prompt gamma (Fig. 1). Imaging of the patient was performed using a dedicated modular J-PET scanner, equipped with the acquisition system enabling simultaneous registration of signals from annihilation photons and prompt gamma. The sensitivity of the modular J-PET for the detection of two-photon events is ~57 times higher than that for simultaneous detection of two-photons and prompt gamma (see detailed description in Discussion). Taking into account the branching ratio of prompt gamma emission in the decay of ^{68}Ga, the rate of recorded events useful for two-photon PET imaging is over 4000 times higher than the rate of events useful for positronium imaging, which was a great challenge in the presented research.

Here, we applied the recently introduced positronium imaging method (*9*, *10*) that was recently successfully validated in the first ex vivo positronium imaging of phantoms comprising cardiac myxoma tumor and healthy adipose tissues operated from patients (*8*). The observed dependence of the mean positronium lifetime on the tissues type (*6*, *16*, *35*–*37*) and on the grade of cancer malignancy (*5*) encourages one to perform in vivo positronium imaging to test the hypothesis if positronium may serve as a parameter in the in vivo diagnosis in clinics. This study presents the clinical positronium lifetime images and a discussion of the prospects of its application in clinical imaging with total-body PET scanners.

RESULTS

The main result of the presented research is the demonstration of the in vivo image of positronium lifetime in the human head. The research was performed in such a way as not to interfere with routine diagnostics and therapy. The examined patient was a 45-year-old man with a recurrent secondary glioblastoma (II/IV) in the right frontoparietal lobe. The primary aim of the conducted therapy was to destroy the glioma tumor using α particles emitted by the ^{225}Ac radionuclide. The demonstration of positronium imaging was possible thanks to the concurrent theranostic application of the ^{68}Ga isotope to monitor the site of cancer lesions using a PET scanner. The study protocol, approved by the Ethical Committee of the Medical University of Warsaw, is presented pictorially in Fig. 2A, indicating the diagnosis and treatment workflow.

In the first step, the location of the glioblastoma tumor was determined by administering a radiopharmaceutical [^{68}Ga]Ga-PSMA-11 to the patient in a dose of 178 megabecquerel (MBq) (*14*, *26*) and using a PET/computed tomography (CT) Biograph

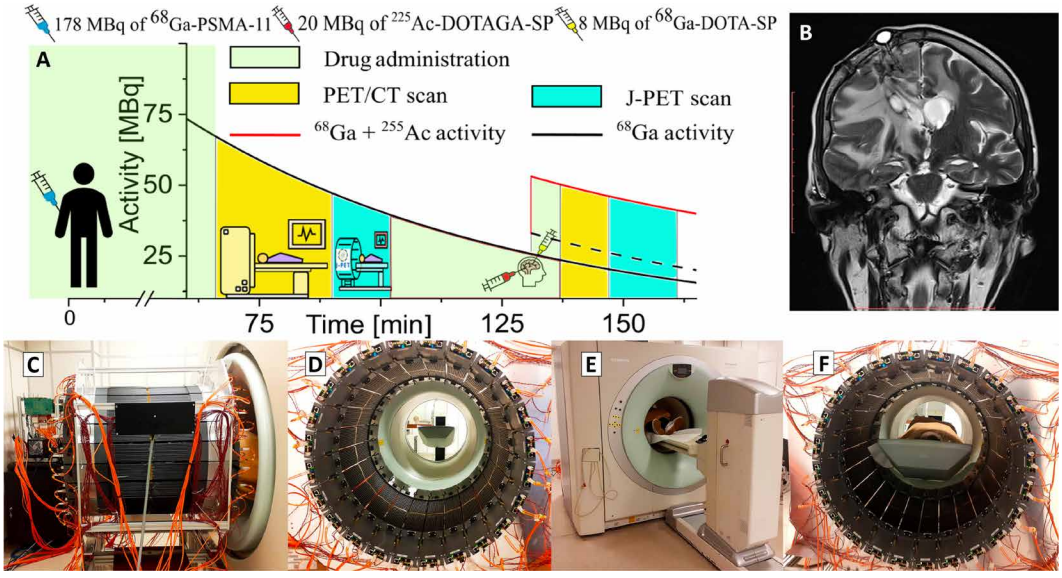

Fig. 2. Course of diagnosis and treatment of a patient with secondary recurrent glioblastoma. (**A**) The solid black curve indicates the decrease in the activity of the ^{68}Ga radionuclide after intravenous injection of a 178-MBq activity of the [^{68}Ga]Ga-PSMA-11 radiopharmaceutical followed 131 min later by intratumoral administration of 8 MBq of [^{68}Ga]Ga-DOTA-SP (black dashed curve) together with 20 MBq of [^{225}Ac]Ac-DOTAGA-SP (red curve). After the first and the second administration of pharmaceuticals, the patient was imaged with the Siemens PET/CT Biograph 64 TruePoint and then with a modular J-PET for the time indicated in the graph in yellow and turquoise, respectively. (**B**) The T2-weighed MRI coronal image of the head (Magnetom 3T, Siemens Healthcare) showing the tumor and the position of the cat-cath system (visible on the upper left part of the head) for the administration of a radiopharmaceutical for the local treatment of glioblastoma. (**C** to **F**) Photographs illustrating the course of patient imaging with the modular J-PET scanner. (C) Modular J-PET scanner placed behind the PET/CT Biograph 64. (D) View of the patient's bed from the inside of the J-PET tomograph. (E) The patient was moved on the table so that the torso and legs were in the Biograph PET/CT and the head in the J-PET scanner. In this view, only the patient's feet are visible on the edge of the Biograph PET/CT. (F) Photograph of the patient with the head inside of the J-PET scanner during imaging after intravenous administration of the [^{68}Ga]Ga-PSMA-11 radiopharmaceutical.

64 TruePoint scanner. PSMA is a prostate-specific membrane antigen expressed in tumor-associated vessels (*14*, *38*). Immediately afterward, the patient was moved on the table to the J-PET tomograph for a 10-min DAQ for comparison to the PET/CT image and to establish a baseline for the J-PET scanner. The patient's examination is documented in the photographs in Fig. 2 (C to F). Immediately afterward, a treatment step was carried out. Using a catheter connected to a subcutaneous port implemented into a postoperative cavity [see magnetic resonance imaging (MRI) image in Fig. 3B] (*39*), the patient was injected intracavitary (locally) with 20 MBq of ^{225}Ac-labeled substance P ([^{225}Ac]Ac-DOTAGA-SP) together with ^{68}Ga-labeled substance P ([^{68}Ga]Ga-DOTA-SP) at the dose of 8 MBq. Substance P having a high affinity to the neurokinin-1 receptors (overexpressed on the glioblastoma cells surface and within the tumor neovasculature) was used to deliver α particle emitter ^{225}Ac to the tumor cells (*40*). The therapy was performed as previously optimized and described in (*39*), and the ^{225}Ac dose activity was chosen as a compromise between the therapeutic effect and the side reaction for the treatment (*41*). During the treatment stage, the pharmaceutical [^{68}Ga]Ga-DOTA-SP labeled with the radionuclide ^{68}Ga was also used to monitor the accumulation sites of substance P and thereby verify the administration of the ^{225}Ac radionuclide to the glioma tumor. The obtained PET/CT images demonstrate the highest accumulation of the pharmaceutical [^{68}Ga]Ga-DOTA-SP in the tumor cavity (Fig. 3, A to C), confirming the correct delivery of the ^{225}Ac radionuclide

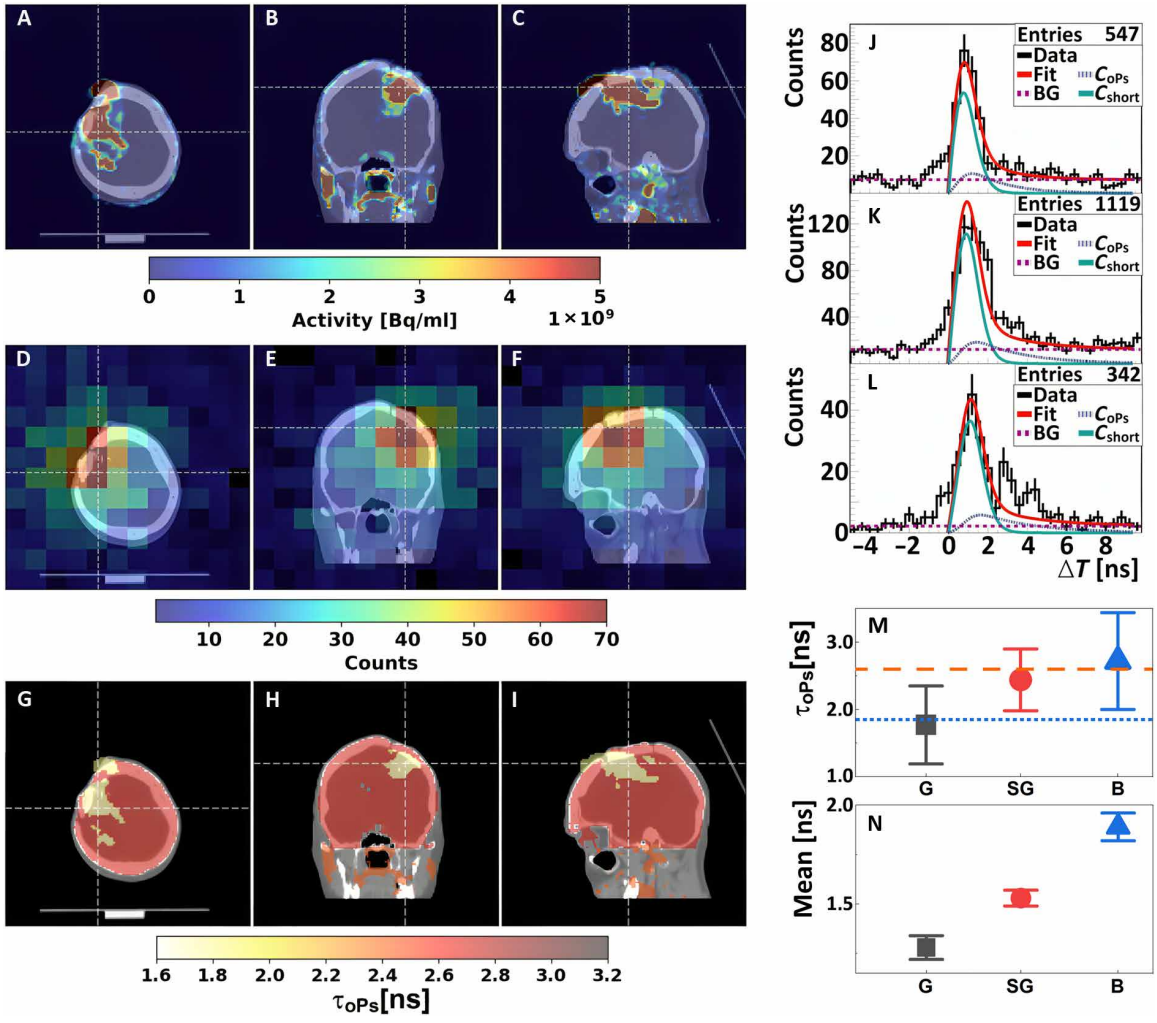

Fig. 3. Positronium images of the head of a patient with recurrent secondary glioblastoma in the right frontoparietal lobe. (**A** to **C**) Standard PET/CT images obtained with Biograph 64 TruePoint. An accumulation of [^{68}Ga]Ga-DOTA-SP in the capsule and cavity of the tumor in transverse (A), coronal (B), and sagittal (C) planes is presented. (**D** to **F**) Images of the density distribution of positron annihilation accompanied by the emission of the prompt gamma are shown in transverse (D), coronal (E), and sagittal (F) planes. These images were acquired with the J-PET tomograph. The white thin dashed lines in each (A) to (F) image indicate a cross section with the other two planes presented. (**G** to **I**) Positronium images shown in transverse (G), coronal (H), and sagittal (I) planes. (**J** to **L**) Distributions of positron annihilation lifetime (Δ*T*) determined in the glioblastoma tumor (J), salivary glands (K), and healthy brain tissues (L). Black histograms denote experimental data. The superimposed curves indicate the result of the fit of the function describing contributions from oPs (C_{oPs}), from pPs and direct annihilations (C_{short}), and from the background due to accidental coincidences (BG). The red curve denotes the sum of all contributions (Fit). (**M** and **N**) Mean oPs lifetime [τ_{oPs}; (M)] and mean value of the positron lifetime in the range between 0 and 5 ns [Mean; (N)] determined for the glioblastoma tumor (G; black squares), salivary glands (SG; red circles), and healthy brain tissues (B; blue triangles). The blue dotted line and orange dashed line indicate the mean oPs lifetime in cardiac myxoma tumor (1.92 ns) and adipose tissue (2.72 ns) (*6*).

to the glioma. The images also indicate accumulation in the salivary glands because they are composed of cells that express receptors on their cell membranes showing a high affinity for PSMA (*14*), and PSMA was used in the first step of the procedure. Once this monitoring step was completed, the patient was moved on the table to the modular J-PET tomograph for the 13-min DAQ for positronium imaging.

A dedicated modular J-PET scanner is built from 24 detection modules (*18*) each constructed from plastic scintillators (*42*) and programmable electronics (*19*). The scanner, seen in photographs in Figs. 1A and 2 (C to E), is described in detail in Methods. The data were collected using a DAQ system that we developed, which enabled triggerless signal acquisition (*20*). The continuous triggerless data recording allowed us to collect multiphoton coincidences. Recorded data were analyzed using a dedicated J-PET programming framework (*43*). The data analysis procedures, background subtraction, and positronium image reconstruction are described in detail in Methods. Therefore, it will only be mentioned briefly in the following.

In the first step of the analysis, the data were decoded from electronics to timestamp format, and then the recorded timestamps were used to reconstruct the registered signals. In the next step of the low-level data processing, signals were used to reconstruct the time and position of each gamma photon interaction in the tomograph. Furthermore, the signals from annihilation photons and prompt gamma were disentangled and grouped into events. An event is referred to as the entire sequence of processes occurring in the patient's body and the tomograph as a result of the decay of a single radionuclide. For each event, comprising two annihilation photons and prompt gamma, the annihilation place and time as well as the positron emission time were reconstructed. The set of such selected events (after the suppression of the instrumental and physical background) was used to reconstruct the images of the density distribution of annihilation places associated with the emission of the prompt gamma (Fig. 3, D to F).

Because of the low fraction of such events [only 1.3% in the case of ^{68}Ga (Fig. 4B)], the images are characterized by low statistics. Therefore, to determine the positronium lifetime, the reconstructed image of the head of the patient was divided only into three regions of interest: the range around the glioma cancer (G), the healthy brain tissues (B), and the area around the salivary glands (SG). The lifetime spectra determined for these regions are shown in Fig. 3 (J to L), respectively.

The superimposed violet dotted curve indicates contribution due to the annihilation intermediated by oPs. Possible annihilation mechanisms are depicted in Fig. 1B. The contributions from fast annihilation mechanisms (pPs → 2γ and direct e^+e^- → 2γ) and annihilations via oPs (oPs → 2γ) were established by deconvoluting the experimental lifetime spectra by using the dedicated PALS Avalanche software (*44*–*46*). Details of the fitting procedure are described in Methods.

The determined mean oPs lifetimes (τ_{oPs}) are presented in Fig. 3M. One observes a trend in the data. The measured value of the mean oPs lifetime in the glioma tumor (1.77 ± 0.58 ns) falls below the salivary glands (2.44 ± 0.46 ns), which in turn is below the measurement in healthy brain tissues (2.72 ± 0.72 ns). In addition to the mean oPs lifetime, the mean positron lifetime was calculated without performing the fit. The mean positron lifetime was calculated considering distributions shown in Fig. 3 (J to L) in the range between 0 and 5 ns. The resulting values of mean positron lifetime for the glioma, salivary glands, and brain tissues are shown in Fig. 3N. The determined values are equal to 1.28 ± 0.06 ns for the glioma tumor, 1.53 ± 0.04 ns for salivary glands, and 1.89 ± 0.06 ns for healthy brain tissues. Notably, the differences between different tissues in the mean positron lifetimes visible in Fig. 3N are more statistically pronounced than differences in the mean oPs lifetimes presented in Fig. 3M. This

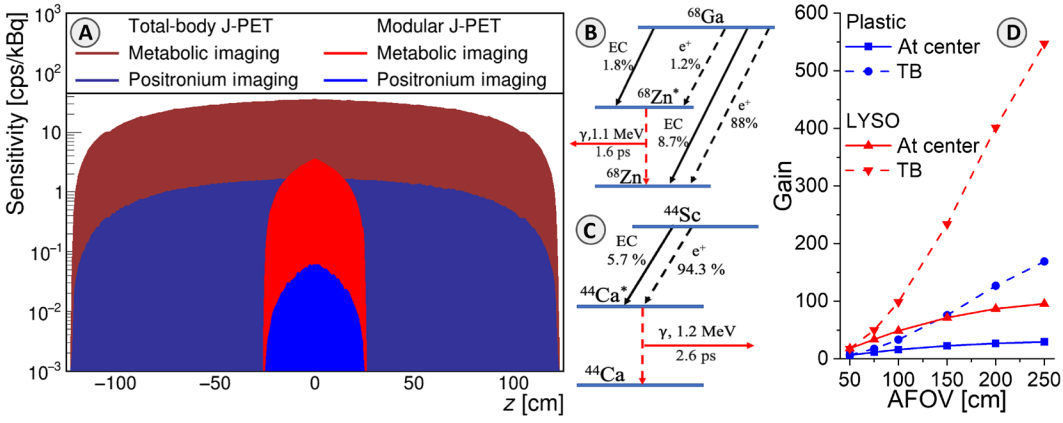

Fig. 4. Comparison of positronium and standard PET imaging sensitivities. (**A**) Positronium imaging sensitivity profiles for registration of γγ+γ$_p$ events (blue) are compared to sensitivity profiles for standard PET metabolic imaging based on registration of γγ events (red). Sensitivity profiles of modular J-PET applied in this study are shown together with the sensitivity profiles for the design of the total-body J-PET with 250-cm AFOV (*50*, *84*). (**B**) Decay scheme of the ^{68}Ga radionuclide. EC denotes the electron capture, while "e^+" denotes the emission of a positron. The mean lifetime of the excited nucleus ^{68}Zn* and the energy of the deexcitation (prompt) gamma are indicated. In this research, the $^{68}Ga \rightarrow {}^{68}Zn^* + e^+ + \nu \rightarrow {}^{68}Zn + \gamma_p + e^+ + \nu$ decay chain was used, occurring only in about 1.3% of all e^+ emissions. (**C**) Decay scheme of the ^{44}Sc radionuclide, the most suited isotope for positronium imaging (*50*, *51*, *85*). In ^{44}Sc decay, the emission of positron is accompanied by the prompt gamma in 100% cases. (**D**) Estimated gain of positronium imaging sensitivity by increasing the AFOV with respect to the modular J-PET used in this research. The gain is calculated for the sensitivity at the center (solid lines) and for the whole-body positronium imaging (dashed lines). Results for standard crystal-based PET systems (based on the uEXPLORER) are shown in red, and the result for the J-PET based on plastic scintillators is shown in blue. The sensitivity at the center for positronium imaging would increase by a factor of 28 for the total-body J-PET and by a factor of 87 for uEXPLORER with AFOV = 194 cm (*25*).

positron lifetime measurement in healthy brain tissues is 7 SDs greater than the value found in the glioma tumor and 5 SDs greater than the value for salivary glands. Combining information about the annihilation density distributions (Fig. 3, A to C), reconstructed density distributions of e^+e^- annihilations associated with the prompt gamma emission (Fig. 3, D to F), and the mean oPs lifetimes (Fig. 3M), the positronium lifetime image of the examined patient is determined as shown in Fig. 3 (G to I). Details are described in Methods.

DISCUSSION

This manuscript presents the in vivo demonstration of positronium imaging. Figure 3 displays images of the mean oPs lifetime in the brain of a patient with a glioma tumor. The images were obtained using the ^{68}Ga radionuclide attached to PSMA-11 and substance P, two different molecules that show high specificity for glioma: substance P by binding to receptors on the surface of glioma cells and PSMA-11 by binding to a receptor found on microvascular endothelial cells in the glioma tumor. The registration of photons from positronium annihilation was used to reconstruct the location and time of positronium decay, while the prompt gamma emitted by the ^{68}Ga isotope was used to determine the time of positronium formation. This in vivo imaging was made possible by the specially designed and constructed multiphoton J-PET scanner, which facilitates the simultaneous registration and identification of annihilation photons and prompt gamma rays. The J-PET scanner used in this study was constructed as a lightweight (60 kg), modular, and portable system, enabling its straightforward installation (taking less than 1 min) around the patient's bed.

The mean oPs lifetime observed in healthy brain tissues (2.72 ns ± 0.72 ns) differs from that observed in glioma tumors (1.77 ns ± 0.58 ns), suggesting the potential of positronium imaging to enhance the specificity of PET diagnosis in in vivo tissue pathology assessment. While presently a 1 SD effect, the in vivo determined mean oPs lifetime in glioma tumors is comparable to the previously determined ex vivo lifetime in cardiac myxoma tumors (1.92 ± 0.02 ns), while the mean oPs lifetime in the healthy brain is similar to the ex vivo values obtained for healthy adipose tissues (2.72 ± 0.05 ns) (*6*, *8*).

The uncertainties in this in vivo investigation are substantial due to the limited number of registered events (e.g., only 86 oPs annihilations were identified in the glioma). However, it is crucial to emphasize that the sensitivity of positronium imaging can be substantially enhanced compared to the modular J-PET used in this study by using total-body PET scanners with an extended axial field of view (AFOV). Figure 4D shows that the sensitivity for positronium imaging will increase by a factor of 28 for the total-body J-PET and by a factor of 87 for uEXPLORER with AFOV = 194 cm (*25*). On the basis of this figure, we can also roughly estimate that it will increase by a factor of about 50 for Siemens Quadra with AFOV = 106 cm (*47*) and by a factor of about 70 for uPennPET Explorer with AFOV = 142 cm (*48*). Two of the mentioned total-body PET systems [Siemens Quadra (*49*) and uPennPet Explorer (*48*)] have DAQ capabilities that would enable positronium imaging. Moreover, the effective sensitivity can also be substantially increased by applying other $\beta^+\gamma$ emitters than ^{68}Ga, such as ^{14}O, ^{44}Sc, ^{82}Rb, or ^{124}I (*50*–*52*). Of these, the use of ^{44}Sc would best improve imaging efficiency as it emits the prompt gamma 100% of the time after positron emission compared to only 1.34% for ^{68}Ga (*50*). The decay schemes of ^{68}Ga and ^{44}Sc are shown in Fig. 4 (B and C), respectively. The ^{44}Sc radionuclide has already been applied in phantom (*53*) and preclinical PET imaging (*54*) using folates (*55*, *56*), somatostatin analogs (*57*), and PSMA ligands (*58*, *59*). It can be produced using accelerators (*59*–*61*) or using the ^{44}Ti/^{44}Sc generator (*62*). The application of the ^{44}Sc radionuclide and total-body PET systems would enable positronium imaging with thousands of times greater sensitivity compared to the first images presented in this work (Fig. 3). The sensitivity will increase by ~3700, 5200, or 6500 times when using Siemens Quadra, uPenn Explorer, or uEXPLORER, respectively. This will enable the acquisition of millions of events with coincident registration of annihilation photons and prompt gamma rays, a number comparable to standard PET imaging. Such high event statistics will enable the effective application of recently developed iterative positron imaging reconstruction methods (*63*–*66*), which can improve the spatial resolution of positronium lifetime images to less than 4 mm (*63*, *64*). The time resolution of determining the mean oPs lifetime (τ_{oPs}) scales inversely proportional to the square root of the number of identified oPs events (*8*, *11*). Hence, by extrapolating the result obtained in this study, we anticipate that the use of the high-sensitivity scanners mentioned above will enable τ_{oPs} imaging with a temporal resolution better than 10 ps, which can potentially be further improved using iterative methods (*15*). It is worth noting that a temporal resolution of 20 ps was already achieved in the first ex vivo positronium imaging (*8*) and that other methods for improving the precision of lifetime spectra analysis are actively being developed (*15*, *63*–*68*).

The resolution of 10 ps is much smaller than the range of oPs lifetime values for various tissues, ranging from about 1.4 to 2.9 ns (*6*, *16*, *35*–*37*, *69*). It is also smaller than differences observed in the mean oPs lifetime between healthy and cancer tissues, ranging from 50 to 700 ps (*5*, *6*, *8*, *17*, *70*, *71*). Consequently, the advent of positronium imaging with a 10-ps resolution, which is achievable by total-body PET systems, may be useful for the in vivo assessment of tissue pathology. Such accuracy of oPs lifetime imaging could, in principle, enable the use of positronium as a biomarker of hypoxia to distinguish between hypoxic and normoxic states in tissue in vivo. The partial pressure of oxygen in cancerous tissues is ~10 to 50 mmHg lower than that in healthy tissues, depending on the tissue type (*3*, *72*). The changes in oPs lifetime in the tissues of living organisms due to variations in oxygen pressure are not yet known. In water, these changes are very small, at the level of a few picoseconds (*3*, *4*, *34*). However, in cells, they are expected to be on the order of 50 ps, based on the analogy with the change in mean oPs lifetime in organic liquids (*4*, *34*) such as isopropanol, which has a structure very similar to that of many typical cell metabolites. In isopropanol, the mean oPs lifetime (via the conversion mechanism shown in Fig. 1) changes by about 50 ps when the oxygen pressure changes by 10 mmHg (*4*, *34*).

Notably, results shown in Fig. 3N demonstrate that the determined mean positron annihilation lifetime exhibits statistically significant differences between glioma (1.28 ± 0.06 ns), salivary glands (1.53 ± 0.04 ns), and healthy brain tissues (1.89 ± 0.06 ns). The mean positron lifetime denotes the average time between positron emission and annihilation, averaged over all possible annihilation mechanisms (illustrated in Fig. 1). Consequently, it can be interpreted as an effective parameter reflecting both the intramolecular void

size and oxygen concentration (primarily detected by oPs) and bulk molecular structure (primarily influencing direct annihilation). Although the mean positron lifetime is less sensitive to partial oxygen pressure than the oPs lifetime, its determination is simpler (merely averaging lifetimes without requiring deconvolution of the lifetime spectrum) and may prove more robust for clinical applications as a measure of bulk molecular alterations.

Last, it is noteworthy that positronium imaging provides complementary information about the inter- and intramolecular structure and the degree of tissue oxidation compared to the information about metabolic rate (e.g., fluorodeoxyglucose uptake), anatomy (electron density), and morphology (hydrogen density) currently attainable with PET, CT, and magnetic resonance tomography, respectively (*8*). The diagnostic potential of positronium images remains to be fully explored by establishing an in vivo correlation between the lifetime of positronium and positrons in tissues and the degree of tissue alterations. At present, we may only hypothesize that positronium imaging may become an early diagnostics indicator for neurodegenerative diseases such as dementia, Alzheimer's disease, and Parkinson's disease. We find this potential possibility as very exciting. Here, we take a step in this direction by demonstrating positronium imaging of the human brain in vivo.

PET, with its unparalleled imaging sensitivity, has revolutionized the field of precision medicine (*23*, *40*).

We envision that positronium imaging could transcend the current PET diagnostic paradigm, paving the way for assessment of subnanometer-scale cellular structures in vivo tissue (*1*).

METHODS

Description of the patient, bioethical committee

The imaging study involving the "Clinical application of the prototype J-PET apparatus" was performed at the Department of Nuclear Medicine of the Medical University of Warsaw in March 2022. The study was approved by the Ethical Committee at the Medical University of Warsaw (opinion from 21 February 2022, no. KB/16/2022). Informed consent was obtained from the patient to enter the study and to publish the results. The examined patient was a man aged 45, diagnosed in 2013 with a grade II primary brain glioma according to the WHO CNS5 classification (*73*). The tumor is located in the right frontoparietal lobe. In further histopathological examination performed in 2021, the brain tumor was classified as grade IV. The SUV_{max} value of 8.4 was determined in the study presented in this manuscript. The volume of the glioma tumor calculated at the 10% cutoff of the SUV_{max} value is equal to 97 ml.

Radiopharmaceutical preparation

The $^{68}Ge/^{68}Ga$ GalliaPharm generator (Eckert & Ziegler, Germany) was used for all ^{68}Ga labeling. Radiopharmaceutical preparation of [^{68}Ga]Ga-PSMA-11 is described in detail in (*14*) and [^{68}Ga]Ga-DOTA-SP in (*74*). The preparation of therapeutic doses of [^{225}Ac]Ac-DOTA-SP is described in (*39*).

^{68}Ga radionuclide

In the presented studies, the ^{68}Ga radionuclide was used for imaging. ^{68}Ga emits positrons with a maximal (average) energy of 1.899 MeV (0.830 MeV), which is substantially larger than the maximal (average) energy of positrons emitted by the ^{18}F radionuclide, amounting to 0.634 MeV (0.25 MeV) (*75*). Here, we compare the properties of ^{68}Ga and ^{18}F radionuclides as ^{18}F is most commonly used in clinical PET imaging (*23*).

In the case of ^{68}Ga, the average and maximum ranges of positrons in water are $R_{mean} \simeq 2.9$ mm and $R_{max} \simeq= 8.5$ mm, respectively, and are much larger compared to $R_{mean} \simeq 0.6$ mm and $R_{max} \simeq 2.4$ mm for positrons emitted by ^{18}F (*75*–*77*). The finite range of positrons leads to a deterioration of the spatial resolution of PET images. Using a small preclinical PET system, where the smearing due to the noncolinearity of annihilation photons is suppressed, it was shown that the increased range of positrons emitted from ^{68}Ga worsens the spatial resolution of PET images from 1.67 mm [full width at half maximum (FWHM)] for ^{18}F to 2.5 mm (FWHM) for ^{68}Ga (*78*) when imaging a 1.3-mm-diameter hole in the phantom. Consistently, for imaging with a microPET system using filled capillary tubes of 1 mm in diameter, the spatial resolution for PET imaging of tissues changes from ~1.9 mm (FWHM) for ^{18}F to ~2.8 mm (FWHM) for ^{68}Ga (*75*). Thus, the additional blurring due to the positron range in the tissue increases from about 0.3 mm for ^{18}F to about 1 mm for ^{68}Ga (*75*). Therefore, we may neglect this effect in the presented studies where the resolution of the first direct positronium images is still on the order of a few centimeters.

Description of PET/CT

PET/CT examinations were performed using a Biograph 64 TruePoint PET/CT scanner (Siemens Medical Solutions, Knoxville, TN). The course of imaging is shown in Fig. 2A. Data were acquired in the three-dimensional (3D) mode. CT data were used for the attenuation and scatter correction as provided by the vendor. The reconstruction was performed using the TrueX algorithm (Siemens Medical Solutions) with point spread function modeling, 3 iterations, and 21 subsets. Postreconstruction 3D Gaussian filtering was performed with FWHM = 4 mm.

Description of the modular J-PET tomograph

The modular J-PET scanner (Fig. 5), used in the presented research, is the portable PET tomograph consisting of 24 independent detection modules, where each module is composed of 13 axially arranged plastic scintillator strips with dimensions of 24 × 6 × 500 mm^3. A single module constitutes an independent detection unit composed of scintillator strips coupled to the front-end electronics board that transfers digitized information about the registered signals to the DAQ system (via optical links visible as orange cables in Figs. 1 and 2). The modular J-PET system, with visible scintillator strips and electronics boards, is shown in a photograph in Fig. 5A. The detection modules are lightweight (~2 kg each), can be arranged in various configurations, and can be easily moved within the diagnostic room. For this research, they were arranged in a cylinder with an inner diameter of 74 cm and positioned behind the Biograph 64 TruePoin PET/CT scanner as can be seen in Fig. 2. The modular J-PET scanner and its performance, encompassing signal reconstruction, event reconstruction, and event selection procedures, are comprehensively detailed in (*18*). For the sake of manuscript completeness, only a concise overview of the most important features is provided herein.

Plastic scintillator strips (Saint Gobain BC-404) are wrapped in Vikuiti enhanced specular reflector foil to improve light propagation and DuPont Kapton 100B film to ensure light tightness (*42*). At the ends of each scintillator strip, on both 24 × 6 mm^2 surfaces, four Hamamatsu-S13 silicon photomultipliers (SiPMs), with the area of 6 × 6 mm^2, are connected optically by using the Saint-Gobain BC-600

optical cement. The gamma ray emitted from the patient induces in the scintillator optical photons, which are converted to electric signals by eight SiPMs. The bias voltage at all SiPM is set to 56 V. SiPM signals are amplified (x13) and sampled at the two voltage levels of 30 and 70 mV (see Fig. 6C) using dedicated front-end electronics boards, described in detail in (*19*). As a result of gamma photon interaction in a scintillator strip, two timestamps are recorded at the leading and two timestamps at the trailing edge on each signal from the eight SiMPs. Timestamps recorded by the front-end electronics are collected in the continuous mode (referred to as triggerless or single interaction mode) by the dedicated DAQ system described briefly in the next section, while for details, the reader is referred to (*20*). The possibility of triggerless recording makes the modular J-PET the multiphoton scanner, enabling simultaneous detection of annihilation photons (2γ) and prompt gamma (γ_p). Figure 4A shows the sensitivity profile of the modular J-PET scanner for standard 2γ PET imaging (red) and for $2\gamma + \gamma_p$ positronium imaging (blue). At the center, the sensitivity for 2γ PET imaging amounts to 3.4 counts per second (cps)/kilobecquerel (kBq), while the sensitivity for $2\gamma + \gamma_p$ imaging is equal to 0.06 cps/kBq.

DAQ system

The DAQ system is designed to register multiphoton events. Examples of such events useful for positronium imaging are shown in Fig. 6 (A and B). The complete J-PET DAQ system is based on field-programmable gate array electronics, which allow for an efficient pipelined processing of multiple data streams in real time (*20*). Its architecture is hierarchical with the controller board as the central point, concentrator boards as hubs, and end points that are digitizing boards located on the detector modules. The communication between the system components is implemented on optical link

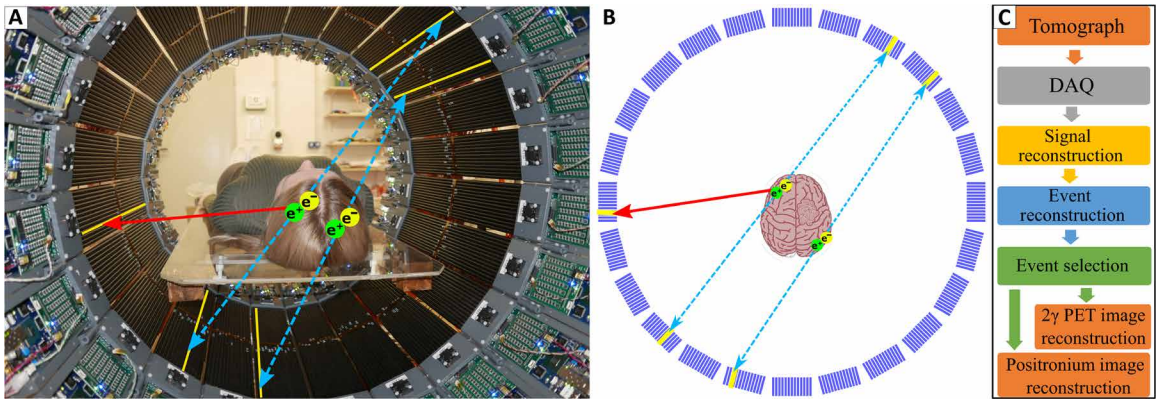

Fig. 5. Modular J-PET tomograph. (**A**) Photograph of the modular J-PET system with a human placed inside the scanner. The superimposed blue dashed arrows indicate photons from the electron-positron annihilation ($e^+e^- \rightarrow \gamma\gamma$), while the red solid arrow indicates prompt gamma (γ_p) from the decay of the ^{68}Ga radionuclide. The modular J-PET scanner enables registration and identification of both $\gamma\gamma$ and $\gamma\gamma+\gamma_p$ events, which are used in this study for the standard PET imaging ($\gamma\gamma$) and positronium imaging ($\gamma\gamma+\gamma_p$). (**B**) Cross section of the modular J-PET showing the 24-module structure of the scanner, where each module is composed of 13 scintillator strips. Scintillators that register the photons are marked in yellow in (A) and (B). (**C**) Block diagram of the data processing (*43*). Light signals generated by gamma photons in the tomograph are collected by a triggerless DAQ system (*20*) and stored on discs in the form of the continuous sequence of timestamps. Timestamps are used for signal reconstruction including the place and time of gamma photon interaction. Signals are then used for event reconstruction. Next, the true $\gamma\gamma$ and $\gamma\gamma+\gamma_p$ events are selected by event selection algorithms. Last, the selected events, in the list mode format, are used for the standard 2γ PET image reconstruction and positronium image reconstruction.

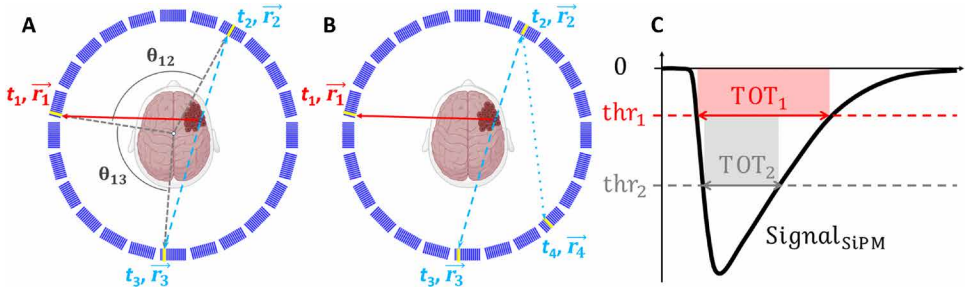

Fig. 6. Pictorial representation of events and signals used for positronium imaging. (**A**) Schematic cross section of the modular J-PET scanner with the superimposed illustration of an exemplary event used for positronium imaging. A deexcitation photon and two annihilation photons are shown as red solid lines and blue dashed lines, respectively. Scintillators that registered photons are marked in yellow. The reconstructed position and time of photons' interaction (hit position and hit time) are indicated as $\vec{r}_i$ and t_i (i = 1, …, 3), respectively. For the purpose of the event selection, the relative angles between photons (θ_{12} and θ_{13}) are calculated with respect to the center as angles in the plane transverse to the scanner axis (*XY* plane), as illustrated in the figure. (**B**) Example of an event with more than three hits, which are also used for positronium imaging. The position and time of interaction of the scattered photon are indicated as ($t_4, \vec{r}_4$). (**C**) Pictorial definition of the TOT for a single SiPM signal. For each SiPM, the timestamps at the leading and trailing edge of the signals are measured at two predefined voltage levels (thresholds): thr_1 and thr_2. This enables us to determine the signal widths at two levels (TOT_1 and TOT_2) and to estimate the area of the signal as $TOT_{SiPM} = thr_1{}^{*}TOT_1 + (thr_2 - thr_1) * TOT_2$. The average of TOT_{SiPM} from eight SiPMs attached to each scintillator is used as a measure of the deposited energy (*81*).

connections with the Xilinx Aurora protocol running at 5 Gigabits per second. A single link is bidirectional and shares three logical functionalities: transport of the measurement data, exchange of control and monitoring messages, and precise time synchronization of the end points. The controller board serves as an interface for the system operator to interact with all components in the system and generates the common synchronization signal that is propagated throughout the system components. The data readout is performed in continuous mode without any sort of hardware trigger. Digitized detector responses are stored in data buffers on the end points and await the synchronization message to arrive. The buffer content is sent back to the concentrators, which aggregate data from multiple end points, encapsulate it into User Datagram Protocol packets, and transfer it out of the system to the storage using a 10–gigabit Ethernet network. The applied DAQ system is described in detail in (*20*).

Signal reconstruction

Raw data collected with the triggerless DAQ (*20*) are stored on discs as a sequence of timestamps determined relative to the synchronization time generated by the DAQ system every 50 μs. The offline processing of signals is conducted using the dedicated programs embedded in the J-PET analysis framework described in detail in (*43*).

The data processing involves assembling timestamps into representations of the SiPM signals and calculating the SiPM signal area (TOT_{SiPM}) as explained in Fig. 6C. Next, for each scintillator strip, the arrival times (t_{left} and t_{right}) of the light signal to the left and right scintillator end are calculated. The arrival times t_{left} and t_{right} are determined as an average of timestamps registered for the leading edge at the lower threshold for four SiPMs attached to the left and right side, respectively. Further on, if the difference between t_{left} and t_{right} times is smaller than 12 ns, then they are considered to originate from the same gamma-ray interaction. The interaction time, referred to as the hit time, is estimated as $t_{hit} = (t_{left} + t_{right})/2$, while the interaction position along the scintillator strip relative to the strip's center is estimated as $z_{hit} = (t_{left} - t_{right}) \times v_s/2$, where v_s denotes the speed of light signal propagation in the scintillator strip. The method is described in detail in (*42*, *79*).

In the above-described estimations of interaction time and position, the corresponding calibration constants were applied individually for each scintillator strip, each SiPM, and each electronic channel. The calibration of all detector components was performed using point-like ^{22}Na and ^{44}Sc radioactive sources and applying methods described in detail in (*8*, *19*, *20*, *79*, *80*).

The energy deposition in a scintillator strip is estimated based on the time-over-threshold value (TOT_{hit}) using the relation established in (*81*), where TOT_{hit} is calculated as an average of TOT_{SiPM} values from SiPMs attached to the scintillator. Figure 7A shows the TOT_{hit} distribution reflecting contributions from continuous

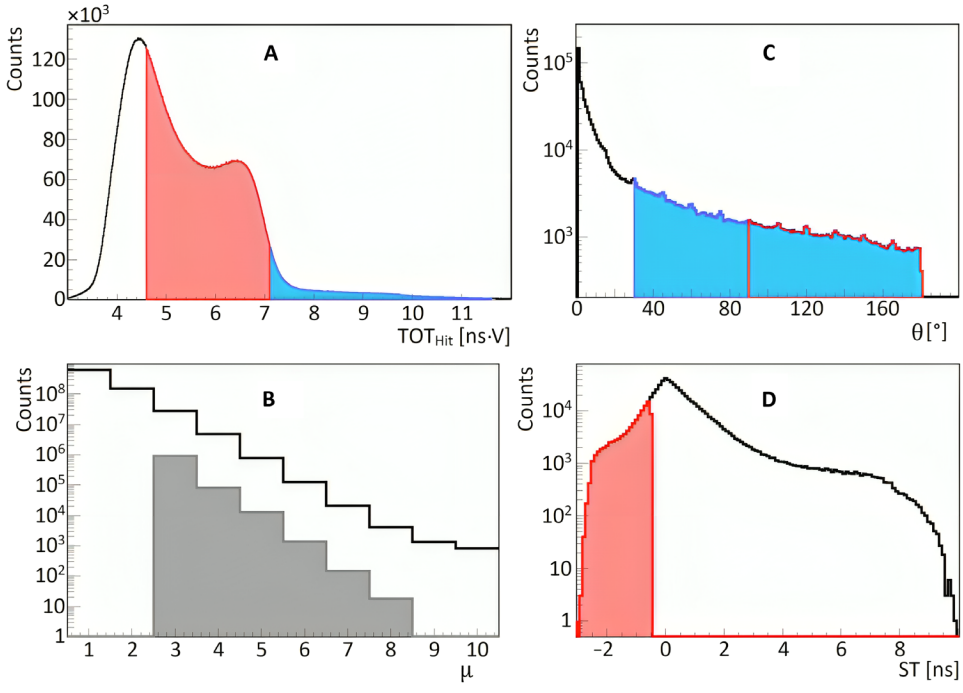

Fig. 7. Event selection criteria for positronium imaging. (**A**) Distribution of TOT (TOT_{Hit}), used for photon identification. The ranges of TOT_{Hit} values for selecting annihilation and deexcitation photons are marked in red and blue, respectively. (**B**) Distribution of a number of hits in the event (hit multiplicity μ). The gray shadowed histogram shows the hit multiplicity for events including one identified deexcitation photon, two identified annihilation photons, and other possible hits identified as scattered photons. (**C**) Distribution of the relative angle (θ) between hit position vectors $\vec{r}_1$, $\vec{r}_2$, ... (defined in Fig. 6A). The figure includes all relative angles in the measured event (θ_{12}, θ_{23}, ...). In the analysis, the relative angle between deexcitation and annihilation photons is restricted to the range marked in blue ($\theta > 30°$), and the red range ($\theta > 90°$) shows the restriction used for the relative angle between annihilation photons. (**D**) Distribution of the ST value used to suppress misidentification of scattered photons as annihilation photons (indicated in Fig. 8A). For hits assigned to annihilation photons [(t_2, $\vec{r}_2$) and (t_3, $\vec{r}_3$)], the ST is defined as a difference between the measured times ($\Delta t = |t_3 - t_2|$) and the time the photon would need to pass from $\vec{r}_3$ to $\vec{r}_2$ ($ST = \Delta t - |\vec{r}_3 - \vec{r}_2| / c$). ST is equal to zero for the scattered photons, while for the annihilation photons, ST is negative. The region used to select events with annihilation photons ($ST < -0.5$ ns) is marked in red. Such selection also reduces a large fraction of events due to the accidental coincidences (as indicated in Fig. 8D) that are spread over the whole range of ST.

energy deposition via Compton scattering of (i) 511-keV annihilation photons, (ii) 1077-keV prompt gamma from ^{68}Ga decay, (iii) photons resulting in scatterings in the detector, and from (iv) photons from decays of oPs and direct annihilations into three photons with energies lower than 511 keV. The continuous spectrum due to 511-keV photons ends (at the so-called Compton edge) at the TOT$_{hit}$ value of about 7 ns · V, while the spectrum due to the 1077-keV prompt gamma extends to higher TOT$_{hit}$ values marked in blue. Prompt gammas are emitted in only about 3% of the ^{68}Ga decays (see decay scheme in Fig. 4B). The TOT hit value is used as a primary criterion to distinguish signals arising from annihilation photons (marked in red) and prompt gamma rays (marked in blue).

Event reconstruction and selection

As an event, we define all processes in the detector system that are due to the single decay of a radionuclide administered to the patient. Signals in scintillator strips (that reconstruction was described in the previous section) are assumed to originate from the same event if their interaction times (t_{hit}) are within a 10-ns time window. Figure 7B shows the distribution of the number of registered interactions per event (distribution of multiplicity of hits in the event). The solid line histogram illustrates that, as anticipated, single-hit events are the most probable, and with each additional hit, the probability of event occurrence decreases by approximately a factor of 5.

For positronium imaging, it is required to select events in which two hits are due to annihilation photons and one hit is due to the prompt gamma as indicated, e.g., in Figs. 1A and 6A. Such selection is performed by requiring two hits with the TOT$_{hit}$ value in the red range defined in Fig. 7A and one hit in the blue range. The gray shadowed histogram in Fig. 7B shows the distribution of hit multiplicity after selecting such events. The multiplicity of hits larger than 3 corresponds to events when the annihilation or prompt photon interacts more than once in the detector. An example of such events is shown in Fig. 6B.

The next step of the data selection aims at the suppression of background events in which the scattered photon was misidentified as an annihilation photon or in which prompt gamma and annihilation photons originate from two different radionuclide decays. Examples of such events are shown in Fig. 8 (A to D). These background events are suppressed by restricting the relative angle θ_{ij} between vectors pointing from the center to the *i*th and *j*th interaction points as defined in Fig. 6A. The experimental distribution of this angle [discussed also in detail in (*81*)] is presented in Fig. 7C. The relative angle between the annihilation photons and prompt gamma is distributed uniformly because they are emitted independently, while the background events with the prompt gamma scattering (Fig. 8A) are at most probable in the adjacent scintillators at small values of θ. Therefore, accepting only events with θ larger than 30° (indicated by the blue range in Fig. 7C) substantially (by a factor of 4) reduces the background from prompt gamma scattering (Fig. 8A), while signal events are reduced only by about 17%. The remaining background from the scattering of the annihilation photons (Fig. 8B) and two types of accidental coincidences (Fig. 8, C and D) was suppressed by further restrictions of the range of the angle θ and by the application of the scatter test (ST) criterion defined in the caption of Fig. 7D. Restricting the angle θ between the annihilation photon candidates to values larger than 90° (range marked in red in Fig. 7C) reduces a large fraction of the background shown in Fig. 8B because the scattering is at most probable in the adjacent scintillators. In addition, it also reduces about 50% of the accidental coincidence of the type shown in Fig. 8D. Notably, this criterion corresponds only to the reduction in the imaging field of view from 74 to 52 cm in diameter and so does not affect the useful signal events. The misidentified background events caused by the scattering of annihilation photons (Fig. 8B) and accidental coincidences (Fig. 8D) with an angle θ greater than 90° are further suppressed using the ST as shown in Fig. 7D and explained in the figure caption.

Events that met all the aforementioned selection criteria were used for the positronium image reconstruction described in the subsequent section. The lifetime spectra depicted in Fig. 3 (J to L) demonstrate that the background under the signal (within the range of 0 to 5 ns) was reduced to a level of ~20%.

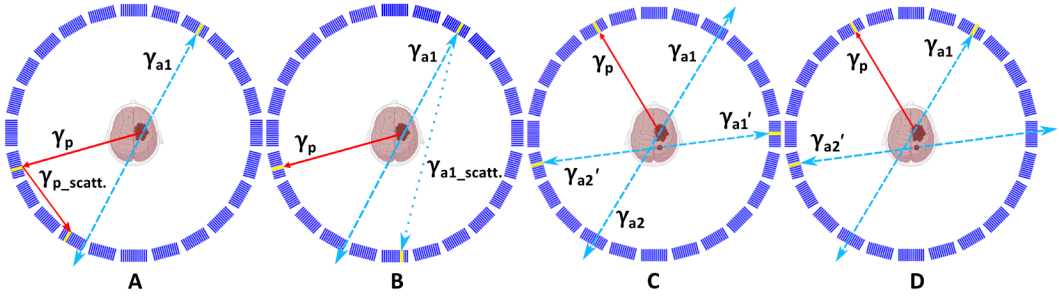

Fig. 8. Topology of background events in positronium imaging with modular J-PET tomograph. Examples of background events superimposed upon the cross section of the modular J-PET scanner. The prompt gamma is represented by a red solid arrow. Primary and scattered annihilation photons are indicated by blue dashed and blue dotted arrows, respectively. Scintillators where photons interacted are highlighted in yellow. (**A**) Example of a background event where one annihilation photon remained undetected while the prompt gamma interacted twice within the detector, leading to the misidentification of the registered scattered photon as the annihilation photon. (**B**) Example of a background event where one annihilation photon remains undetected, while the other annihilation photon interacts twice within the detector, leading to the misidentification of the registered scattered photon as an annihilation photon. Such events can be suppressed using the ST (Fig. 7D). (**C**) Example of the background arising from the accidental coincidence of a prompt gamma from one event and annihilation photons from the other event. A portion of these events can be eliminated using the ST (Fig. 7D). (**D**) Example of the background arising from the accidental coincidence of registering a prompt gamma and one annihilation photon from one event and the other annihilation photon from the other event. A portion of these events can be eliminated by restricting the range of angle θ (Fig. 7C) and by using the ST (Fig. 7D).

Positronium image reconstruction

Selected events comprising hits from prompt gamma $(t_1, \vec{r}_1)$ and from two annihilation photons $[(t_2, \vec{r}_2)$ and $(t_3, \vec{r}_3)]$ are used to reconstruct positronium images by application of the method described in detail in (*8*). In short, the positronium image reconstruction procedure is as follows. For each event separately, the annihilation place $(\vec{r}_a)$ and the positron lifetime in the patient's body (ΔT) are determined. The most probable position $(\vec{r}_a)$ and time (t_a) of positron-electron annihilation is calculated as

$$\vec{r}_a = \frac{\vec{r}_2 + \vec{r}_3}{2} + \frac{c(t_3 - t_2)}{2} \cdot \frac{\vec{r}_2 - \vec{r}_3}{|\vec{r}_2 - \vec{r}_3|} \quad (1)$$

and

$$t_a = \frac{t_2 + t_3}{2} - \frac{|\vec{r}_2 - \vec{r}_3|}{2c} \quad (2)$$

where c denotes the speed of light.

The positron lifetime $(\Delta T = t_a - t_p)$ is next calculated as a difference between annihilation time (t_a) and the time of the positron emission. In the case of the ^{68}Ga radionuclide (as illustrated in the decay scheme in Fig. 4B), the prompt gamma is emitted, on average, only 1.6 ps after the emission of a positron. This extremely short delay can be safely disregarded. Therefore, the time of positron emission is approximated by the time of prompt gamma emission (t_p). The emission time of the prompt gamma is determined by correcting the time of its registration by the time it took to travel from the emission point to the registration point $\vec{r}_1$

$$t_p = t_1 - \frac{|\vec{r}_1 - \vec{r}_a|}{c} \quad (3)$$

In the above calculations, the place of the prompt gamma emission was approximated by the place of positron annihilation. This is justified because, in the case of positrons emitted by the ^{68}Ga radionuclide, the average distance in the tissue between the positron emission and annihilation is equal to about 2.3 mm (*52*), which is small with respect to the spatial resolution of determining $\vec{r}_1$. The 3D tomography image of places of positron-electron annihilations accompanied by the emission of prompt gamma is determined by calculating the number of annihilation points in each voxel of the head of the patient. The transverse, coronal, and sagittal cross sections of the reconstructed images are shown in Fig. 3 (D to F). The presented positronium image cross sections were selected to clearly visualize annihilations in glioblastoma cancer. Because of the low number of events registered in this study, the patient head was divided only into three regions of interest including glioblastoma cancer (G), salivary glands (SG), and the rest constituting the healthy brain tissues (B). The chosen regions are large and include the scalp and other head tissues. However, due to the high affinity of PSMA and substance P to glioblastoma and salivary glands (*14*, *40*), the signal registered may be well considered as originating predominantly from these tissues. The positron lifetime spectra from these regions of interest are shown in Fig. 3 (J to L), while the mean lifetime of oPs and the mean value of positron lifetime are presented in Fig. 3 (M and N). The method of determining the mean lifetime of oPs in the regions of interest is described in the next section.

Positronium mean lifetime determination

The determined positron lifetime spectra (shown as black histograms in Fig. 3, J to L) were used to estimate the mean lifetime of oPs for each region of interest. In principle, the ΔT spectrum, determined for the tissue, comprises contributions from (*2*) (i) the direct electron-positron annihilations (~60%), (ii) annihilations intermediated by pPs (~10%), (iii) annihilations intermediated by oPs (~30%), and the background from accidental coincidences. All these contributions are smeared due to the experimental resolution. The ΔT resolution of the single measurement of ΔT was estimated to 520 ps (FWHM). The width of the bin in the ΔT spectra is equal to 0.4 ns, which is the value close to the FWHM of the ΔT resolution.

In the first step of the positron lifetime spectrum analysis, the constant background from accidental coincidences was estimated by taking the mean value in the ΔT range: -10 ns $< \Delta T < -5$ ns. In this range of negative ΔT values, only events caused by random coincidences are expected. The obtained values for the background contributions (expressed in counts per bin) are equal to 7.2 ± 0.9 for glioblastoma, 12.2 ± 0.9 for the salivary gland, and 2.20 ± 0.33 for a healthy brain. The background contributions are indicated as violet dotted lines in Fig. 3 (J to L). Next, to estimate the mean oPs lifetime, the sum of exponential contributions convoluted with the experimental resolution was fitted to the experimental spectrum using the dedicated PALS Avalanche software, described in detail in (*44*–*46*). Because of the low statistics of events and the time resolution being several times larger than the average pPs lifetime, only the mean oPs lifetime was considered as a free parameter to ensure the stability of the results. The contributions from pPs and direct annihilations were considered as a single component with a fixed mean lifetime of 0.329 ns and 70% intensity (cyan line in Fig. 3, J to L). These values were determined based on a previous ex vivo study of positronium lifetime in the tissues (*8*). The mean oPs lifetimes obtained from the fit are presented in Fig. 3M. In addition, the mean value of ΔT in the signal region between 0 and 5 ns was calculated. The mean was calculated after subtracting the background. The resulting values of the mean positron lifetime in the studied region of interest are shown in Fig. 3N.

Monte Carlo simulations of sensitivity profiles of the PET scanners

The sensitivity profiles and gains presented in Fig. 4 have been determined using the Geant4 Application for Tomographic Emission (GATE) software version 9.0 (*82*) extended by the J-PET group (https://github.com/JPETTomography/Gate). GATE is the advanced open-source software (www.opengatecollaboration.org) based on the Geant4 toolkit (*83*) and dedicated to Monte Carlo simulations in fields of medical imaging and radiotherapy. In PET imaging, GATE allows for the generation and tracking of radioactive source decays and their products, simulation of the sensitivity to the detection scanners, and data processing. In this study, the emlivermore_polar was the used physics list. The materials and geometries of simulated scanners are described below. The modular J-PET scanner consists of 24 modules arranged into a single-layer ring with 740 mm in inner diameter, where each module is composed of 13 axially arranged plastic scintillator strips with dimensions of $24 \times 6 \times 500$ mm^3. The total-body J-PET consists of seven rings with 830 mm in inner diameter, 330 mm in axial length, and a 20-mm gap in between the rings. The total AFOV was equal to 243 cm. Each ring includes 24 modules, where each module comprises two layers in radial direction formed from 16 plastic scintillator strips (*84*) with dimensions of $30 \times 6 \times 330$ mm^3.

As a material representing the plastic scintillator, the EJ-230 was chosen. For positronium imaging, the simulation included 511-keV annihilation photons and prompt gamma rays with an energy of 1160 keV. An energy deposition between 200 and 350 keV was required for annihilation photons, while an energy deposition greater than 350 keV was required for prompt gamma rays. The coincidence window was set to 4 ns for the modular J-PET scanner and to 4.5 ns for the total-body J-PET scanner.

The crystal-based scanners were simulated using lutetium-yttrium oxyorthosilicate crystals with a thickness of 1.81 cm and a geometrical arrangement similar to that of the uEXPLORER scanner (*25*). The calculations were performed for different numbers of rings, including 2, 3, 4, 6, 8, and 10. For the crystal-based scanners, the coincidence time window was set to 4.5 ns. The energy window for annihilation photons was set to 430 to 645 keV, while for prompt gamma photons, an energy deposition greater than 645 keV was required.

Supplementary Materials

This PDF file includes:

Tables S1 to S4

REFERENCES AND NOTES

1. P. Moskal, B. Jasińska, E. Ł. Stępień, S. D. Bass, Positronium in medicine and biology. *Nat. Rev. Phys.* **1**, 527–529 (2019).
2. S. D. Bass, S. Mariazzi, P. Moskal, E. Stępień, *Colloquium*: Positronium physics and biomedical applications. *Rev. Mod. Phys.* **95**, 021002 (2023).
3. P. Moskal, E. Ł. Stępień, Positronium as a biomarker of hypoxia. *Bioalgorithms Medsystem* **17**, 311–319 (2021).
4. K. Shibuya, H. Saito, F. Nishikido, M. Takahashi, T. Yamaya, Oxygen sensing ability of positronium atom for tumor hypoxia imaging. *Commun. Phys.* **3**, 173 (2020).
5. H. Karimi, P. Moskal, A. Żak, E. Ł. Stępień, 3D melanoma spheroid model for the development of positronium biomarker. *Sci. Rep.* **13**, 1648 (2023).
6. P. Moskal, E. Kubicz, G. Grudzień, E. Czerwiński, K. Dulski, B. Leszczyński, S. Niedźwiecki, E. Ł. Stępień, Developing a novel positronium biomarker for cardiac myxoma imaging. *EJNMMI Phys.* **10**, 22 (2023).
7. S. Vandenberghe, P. Moskal, J. S. Karp, State of the art in total body PET. *EJNMMI Phys.* **7**, 35 (2020).
8. P. Moskal, K. Dulski, N. Chug, C. Curceanu, E. Czerwiński, M. Dadgar, J. Gajewski, A. Gajos, G. Grudzień, B. C. Hiesmayr, K. Kacprzak, Ł. Kapłon, H. Karimi, K. Klimaszewski, G. Korcyl, P. Kowalski, T. Kozik, N. Krawczyk, W. Krzemień, E. Kubicz, P. Małczak, S. Niedźwiecki, M. Pawlik-Niedźwiecka, M. Pędziwiatr, L. Raczyński, J. Raj, A. Ruciński, S. Sharma, Shivani, R. Y. Shopa, M. Silarski, M. Skurzok, E. Ł. Stępień, M. Szczepanek, F. Tayefi, W. Wiślicki, Positronium imaging with the novel multiphoton PET scanner. *Sci. Adv.* **7**, eabh4394 (2021).
9. P. Moskal, Positronium imaging, in *IEEE Nuclear Science Symposium and Medical Imaging Conference* (NSS/MIC) (IEEE, 2019), pp. 1–3.
10. P. Moskal, D. Kisielewska, C. Curceanu, E. Czerwiński, K. Dulski, A. Gajos, M. Gorgol, B. Hiesmayr, B. Jasińska, K. Kacprzak, Ł. Kapłon, G. Korcyl, P. Kowalski, W. Krzemień, T. Kozik, E. Kubicz, M. Mohammed, S. Niedźwiecki, M. Pałka, M. Pawlik-Niedźwiecka, L. Raczyński, J. Raj, S. Sharma, Shivani, R. Y. Shopa, M. Silarski, M. Skurzok, E. Stępień, W. Wiślicki, B. Zgardzińska, Feasibility study of the positronium imaging with the J-PET tomograph. *Phys. Med. Biol.* **64**, 055017 (2019).
11. P. Moskal, D. Kisielewska, R. Y. Shopa, Z. Bura, J. Chhokar, C. Curceanu, E. Czerwiński, M. Dadgar, K. Dulski, J. Gajewski, A. Gajos, M. Gorgol, R. del Grande, B. C. Hiesmayr, B. Jasińska, K. Kacprzak, A. Kamińska, Ł. Kapłon, H. Karimi, G. Korcyl, P. Kowalski, N. Krawczyk, W. Krzemień, T. Kozik, E. Kubicz, P. Małczak, M. Mohammed, S. Niedźwiecki, M. Pałka, M. Pawlik-Niedźwiecka, M. Pędziwiatr, L. Raczyński, J. Raj, A. Ruciński, S. Sharma, S. Shivani, M. Silarski, M. Skurzok, E. Ł. Stępień, S. Vandenberghe, W. Wiślicki, B. Zgardzińska, Performance assessment of the 2γ positronium imaging with the total-body PET scanners. *EJNMMI Phys.* **7**, 44 (2020).
12. M. Hofmann, H. Maecke, A. Börner, E. Weckesser, P. Schöffski, M. Oei, J. Schumacher, M. Henze, A. Heppeler, G. Meyer, W. Knapp, Biokinetics and imaging with the somatostatin receptor pet radioligand ^{68}Ga-DOTATOC: Preliminary data. *Eur. J. Nucl. Med.* **28**, 1751–1757 (2001).
13. B. N. Clarke, PET radiopharmaceuticals: What's new, what's reimbursed, and what's next? *J. Nucl. Med. Technol.* **46**, 12–16 (2018).
14. J. Kunikowska, R. Kuliński, K. Muylle, H. Koziara, L. Królicki, ^{68}Ga-prostate-specific membrane antigen-11 PET/CT: A new imaging option for recurrent glioblastoma multiforme? *Clin. Nucl. Med.* **45**, 11–18 (2020).
15. R. Shopa, K. Dulski, Positronium imaging in J-PET with an iterative activity reconstruction and a multi-stage fitting algorithm. *Bioalgorithms Medsystem* **19**, 54–63 (2023).
16. B. Jasińska, B. Zgardzińska, G. Chołubek, M. Gorgol, K. Wiktor, K. Wysogląd, P. Białas, C. Curceanu, E. Czerwiński, K. Dulski, A. Gajos, B. Głowacz, B. Hiesmayr, B. Jodłowska-Jędrych, D. Kamińska, G. Korcyl, P. Kowalski, T. Kozik, N. Krawczyk, W. Krzemień, E. Kubicz, M. Mohammed, M. Pawlik-Niedźwiecka, S. Niedźwiecki, M. Pałka, L. Raczyński, Z. Rudy, N. G. Sharma, S. Sharma, R. Shopa, M. Silarski, M. Skurzok, A. Wieczorek, H. Wiktor, W. Wiślicki, M. Zieliński, P. Moskal, Human tissues investigation using PALS technique. *Acta Phys. Polon. B* **48**, 1737 (2017).
17. B. Zgardzińska, G. Chołubek, B. Jarosz, K. Wysogląd, M. Gorgol, M. Goździuk, M. Chołubek, B. Jasińska, Studies on healthy and neoplastic tissues using positron annihilation lifetime spectroscopy and focused histopathological imaging. *Sci. Rep.* **10**, 11890 (2020).
18. F. T. Ardebili, S. Niedźwiecki, P. Moskal, Evaluation of modular J-PET sensitivity. *Bioalgorithms Medsystem* **19**, 133–139 (2023).
19. M. Pałka, P. Strzempek, G. Korcyl, T. Bednarski, S. Niedźwiecki, P. Białas, E. Czerwiński, K. Dulski, A. Gajos, B. Głowacz, M. Gorgol, B. Jasińska, D. Kamińska, M. Kajetanowicz, P. Kowalski, T. Kozik, W. Krzemień, E. Kubicz, M. Mohhamed, L. Raczyński, Z. Rudy, O. Rundel, P. Salabura, N. G. Sharma, M. Silarski, J. Smyrski, A. Strzelecki, A. Wieczorek, W. Wiślicki, M. Zieliński, B. Zgardzińska, P. Moskal, Multichannel FPGA based MVT system for high precision time (20 ps RMS) and charge measurement. *J. Instrum.* **12**, P08001 (2017).
20. G. Korcyl, B. C. Hiesmayr, B. Jasinska, K. Kacprzak, M. Kajetanowicz, D. Kisielewska, P. Kowalski, T. Kozik, N. Krawczyk, W. Krzemien, E. Kubicz, P. Bialas, M. Mohammed, S. Niedzwiecki, M. Pawlik-Niedzwiecka, M. Palka, L. Raczynski, P. Rajda, Z. Rudy, P. Salabura, N. G. Sharma, S. Sharma, C. Curceanu, R. Y. Shopa, M. Skurzok, M. Silarski, P. Strzempek, A. Wieczorek, W. Wislicki, R. Zaleski, B. Zgardzinska, M. Zielinski, P. Moskal, E. Czerwinski, K. Dulski, B. Flak, A. Gajos, B. Glowacz, M. Gorgol, Evaluation of single-chip, real-time tomographic data processing on FPGA SoC devices. *IEEE Trans. Med. Imaging* **37**, 2526–2535 (2018).
21. T. Jones, D. Townsend, History and future technical innovation in positron emission tomography. *J. Med. Imaging* **4**, 011013 (2017).
22. G. Brownell, W. Sweet, Localization of brain tumors with positron emitters. *Nucleonics* **11**, 40 (1953).
23. A. Alavi, T. J. Werner, E. Ł. Stępień, P. Moskal, Unparalleled and revolutionary impact of PET imaging on research and day to day practice of medicine. *Bioalgorithms Medsyst.* **17**, 203–212 (2021).
24. R. D. Badawi, H. Shi, P. Hu, S. Chen, T. Xu, P. M. Price, Y. Ding, B. A. Spencer, L. Nardo, W. Liu, J. Bao, T. Jones, H. Li, S. R. Cherry, First human imaging studies with the EXPLORER total-body PET scanner. *J. Nucl. Med.* **60**, 299–303 (2019).
25. B. A. Spencer, E. Berg, J. P. Schmall, N. Omidvari, E. K. Leung, Y. G. Abdelhafez, S. Tang, Z. Deng, Y. Dong, Y. Lv, J. Bao, W. Liu, H. Li, T. Jones, R. D. Badawi, S. R. Cherry, Performance evaluation of the uEXPLORER total-body PET/CT scanner based on NEMA NU 2-2018 with additional tests to characterize PET scanners with a long axial field of view. *J. Nucl. Med.* **61**, 861 (2021).
26. J. Kunikowska, J. Kunikowska, R. Czepczyński, D. Pawlak, H. Koziara, K. Pełka, L. Królicki, Expression of glutamate carboxypeptidase II in the glial tumor recurrence evaluated in vivo using radionuclide imaging. *Sci. Rep.* **12**, 652 (2021).
27. R. Wu, Y. Gao, H. Zhang, Y. Chen, F. Tan, D. Zeng, H. Wan, Y. Yang, J. Gu, Z. Pei, Metabolic assessment of cerebral palsy with normal clinical MRI using ^{18}F-FDG PET imaging: A preliminary report. *Front. Neurol.* **13**, 844911 (2022).
28. A. S. Fleisher, M. J. Pontecorvo, M. D. Devous Sr., M. Lu, A. K. Arora, S. P. Truocchio, P. Aldea, M. Flitter, T. Locascio, M. Devine, A. Siderowf, T. G. Beach, T. J. Montine, G. E. Serrano, C. Curtis, A. Perrin, S. Salloway, M. Daniel, C. Wellman, A. D. Joshi, D. J. Irwin, V. J. Lowe, W. W. Seeley, M. D. Ikonomovic, J. C. Masdeu, I. Kennedy, T. Harris, M. Navitsky, S. Southekal, M. A. Mintun; A16 Study Investigators, Positron emission tomography imaging with [^{18}F]flortaucipir and postmortem assessment of Alzheimer disease neuropathologic changes. *JAMA Neurol.* **77**, 829–839 (2020).
29. M. Uenomachi, K. Shimazoe, H. Takahashi, A double photon coincidence detection method for medical gamma-ray imaging. *Bioalgorithms Medsyst.* **18**, 120–126 (2022).
30. K. Shimazoe, M. Uenomachi, Multi-molecule imaging and inter-molecular imaging in nuclear medicine. *Bioalgorithms Medsystem* **18**, 127–134 (2022).
31. K. Shimazoe, M. Uenomachi, H. Takahashi, Imaging and sensing of pH and chemical state with nuclear-spin-correlated cascade gamma rays via radioactive tracer. *Commun. Phys.* **5**, 24 (2022).
32. R. Zaleski, O. Kotowicz, A. Gorska, K. Zaleski, B. Zgardzinska, Investigation of the ability to detect electrolyte disorder using PET with positron annihilation lifetime spectroscopy. *J. Phys. Chem. B* **127**, 9887–9890 (2023).
33. K. Shimazoe, K. Donghwan, T. Mineo, T. Sato, S. Ohta, T. Tatsumi, A. Sugiyama, K. Yamatsugu, S. Nomura, R. Terabayashi, H. Tomita, T. Sonoda, Y. Shigekawa, T. Yokokita,

M. Uenomachi, pH dependence of perturbed angular correlation in DOTA chelated ^{111}In measured with ring-shape gamma-ray detectors. *Interactions* **245**, 22 (2024).
34. P. S. Stepanov, F. A. Selim, S. V. Stepanov, A. V. Bokov, O. V. Ilyukhina, G. Duplâtre, V. M. Byakov, Interaction of positronium with dissolved oxygen in liquids. *Phys. Chem. Chem. Phys.* **22**, 5123–5131 (2020).
35. T. Ahn, D. W. Gidley, A. W. Thornton, A. G. Wong-Foy, B. G. Orr, K. M. Kozloff, M. M. Banaszak Holl, Hierarchical nature of nanoscale porosity in bone revealed by positron annihilation lifetime spectroscopy. *ACS Nano* **15**, 4321–4334 (2021).
36. Y. Jean, Y. Li, G. Liu, H. Chen, J. Zhang, J. E. Gadzia, Applications of slow positrons to cancer research: Search for selectivity of positron annihilation to skin cancer. *Appl. Surf. Sci.* **252**, 3166–3171 (2006).
37. H. Chen, J. van Horn, Y. Jean, Applications of positron annihilation spectroscopy to life science. *Defect Diffus. Forum* **331**, 275–293 (2012).
38. A. G. Wernicke, M. A. Edgar, E. Lavi, H. Liu, P. Salerno, N. H. Bander, P. H. Gutin, Prostate-specific membrane antigen as a potential novel vascular target for treatment of glioblastoma multiforme. *Arch. Pathol. Lab. Med.* **135**, 1486–1489 (2011).
39. L. Królicki, F. Bruchertseifer, J. Kunikowska, H. Koziara, D. Pawlak, R. Kuliński, R. Rola, A. Merlo, A. Morgenstern, Dose escalation study of targeted alpha therapy with [^{225}Ac] Ac-DOTA-substance P in recurrence glioblastoma—Safety and efficacy. *Eur. J. Nucl. Med. Mol. Imaging* **48**, 3595–3605 (2021).
40. L. Królicki, J. Kunikowska, F. Bruchertseifer, H. Koziara, B. Królicki, M. Jakuciński, D. Pawlak, R. Rola, A. Morgenstern, E. Rosiak, A. Merlo, ^{225}Ac- and ^{213}Bi-substance p analogues for glioma therapy. *Semin. Nucl. Med.* **50**, 141–151 (2020).
41. L. Królicki, F. Bruchertseifer, J. Kunikowska, H. Koziara, B. Królicki, M. Jakuciński, D. Pawlak, C. Apostolidis, S. Mirzadeh, R. Rola, A. Merlo, A. Morgenstern, Safety and efficacy of targeted alpha therapy with ^{213}Bi-DOTA-substance P in recurrent glioblastoma. *Eur. J. Nucl. Med. Mol. Imaging* **46**, 614–622 (2019).
42. P. Moskal, S. Niedźwiecki, T. Bednarski, E. Czerwiński, Ł. Kapłon, E. Kubicz, I. Moskal, M. Pawlik-Niedźwiecka, N. G. Sharma, M. Silarski, M. Zieliński, N. Zoń, P. Białas, A. Gajos, A. Kochanowski, G. Korcyl, J. Kowal, P. Kowalski, T. Kozik, W. Krzemień, M. Molenda, M. Pałka, L. Raczyński, Z. Rudy, P. Salabura, A. Słomski, J. Smyrski, A. Strzelecki, A. Wieczorek, W. Wiślicki, Test of a single module of the J-PET scanner based on plastic scintillators. *Nucl. Instrum. Methods Phys. Res. A* **764**, 317–321 (2014).
43. W. Krzemien, A. Gajos, K. Kacprzak, K. Rakoczy, G. Korcyl, J-PET Framework: Software platform for PET tomography data reconstruction and analysis. *SoftwareX* **11**, 100487 (2020).
44. K. Dulski, B. Zgardzińska, P. Białas, C. Curceanu, E. Czerwiński, A. Gajos, B. Głowacz, M. Gorgol, B. C. Hiesmayr, B. Jasińska, D. Kisielewska-Kamińska, G. Korcyl, P. Kowalski, T. Kozik, N. Krawczyk, W. Krzemień, E. Kubicz, M. Mohammed, M. Pawlik-Niedźwiecka, S. Niedźwiecki, M. Pałka, L. Raczyński, J. Raj, Z. Rudy, N. G. Sharma, S. Sharma, S. Shivani, R. Y. Shopa, M. Silarski, M. Skurzok, A. Wieczorek, W. Wiślicki, M. Zieliński, P. Moskal, Analysis procedure of the positronium lifetime spectra for the J-PET detector. *Acta Phys. Polon. A* **132**, 1637–1641 (2017).
45. K. Dulski, C. Curceanu, E. Czerwiński, A. Gajos, M. Gorgol, N. Gupta-Sharma, B. C. Hiesmayr, B. Jasińska, K. Kacprzak, Ł. Kapłon, D. Kisielewska, K. Klimaszewski, G. Korcyl, P. Kowalski, N. Krawczyk, W. Krzemień, T. Kozik, E. Kubicz, M. Mohammed, S. Niedźwiecki, M. Pałka, M. Pawlik-Niedźwiecka, L. Raczyński, J. Raj, K. Rakoczy, Z. Rudy, S. Sharma, Shivani, R. Y. Shopa, M. Silarski, M. Skurzok, W. Wiślicki, B. Zgardzińska, P. Moskal, Commissioning of the J-PET detector in view of the positron annihilation lifetime spectroscopy. *Hyperfine Interact.* **239**, 40 (2020).
46. K. Dulski, PALS Avalanche—A new PAL spectra analysis software. *Acta Phys. Polon. A* **137**, 167–170 (2020).
47. G. A. Prenosil, H. Sari, M. Fürstner, A. Afshar-Oromieh, K. Shi, A. Rominger, M. Hentschel, Performance characteristics of the Biograph Vision Quadra PET/CT system with a long axial field of view using the NEMA NU 2-2018 standard. *J. Nucl. Med.* **63**, 476–484 (2022).
48. B. Dai, M. E. Daube-Witherspoon, S. McDonald, M. E. Werner, M. J. Parma, M. J. Geagan, V. Viswanath, J. S. Karp, Performance evaluation of the PennPET explorer with expanded axial coverage. *Phys. Med. Biol.* **68**, 095007 (2023).
49. W. M. Steinberger, H. Sari, L. Mercolli, S. Parzych, S. Niedźwiecki, G. Łapkiewicz, P. Moskal, E. Stępień, A. Rominger, K. Shi, M. Conti, Positronium lifetime measurements using ^{82}Rb in a long-axial FOV PET/CT scanner, in *2023 IEEE Nuclear Science Symposium, Medical Imaging Conference and International Symposium on Room-Temperature Semiconductor Detectors (NSS MIC RTSD)* (IEEE, 2023), pp. 1–2.
50. P. Moskal, E. Ł. Stępień, Prospects and clinical perspectives of total-body PET imaging using plastic scintillators. *PET Clin.* **15**, 439–452 (2020).
51. T. Matulewicz, Radioactive nuclei for $\beta^+\gamma$ PET and theranostics: Selected candidates. *Bioalgorithms Medsystem* **17**, 235–239 (2021).
52. M. Das, M. Das, W. Mryka, E. Y. Beyene, S. Parzych, S. Sharma, E. Stępień, P. Moskal, Estimating the efficiency and purity for detecting annihilation and prompt photons for positronium imaging with J-PET using toy Monte Carlo simulation. *Bioalgorithms Medsystem* **19**, 87–95 (2023).
53. S. Ferguson, H. Jans, M. Wuest, T. Riauka, F. Wuest, Comparison of scandium-44 g with other pet radionuclides in pre-clinical PET phantom imaging. *EJNMMI Phys.* **6**, 23 (2019).
54. S. Huclier-Markai, C. Alliot, R. Kerdjoudj, M. Mougin-Degraef, N. Chouin, F. Haddad, Promising scandium radionuclides for nuclear medicine: A review on the production and chemistry up to in vivo proofs of concept. *Cancer Biother. Radiopharm.* **33**, 316–329 (2018).
55. C. Müller, M. Bunka, J. Reber, C. Fischer, K. Zhernosekov, A. Türler, R. Schibli, Promises of cyclotron-produced ^{44}Sc as a diagnostic match for trivalent β^--emitters: In vitro and in vivo study of a ^{44}Sc-DOTA-folate conjugate. *J. Nucl. Med.* **54**, 2168–2174 (2013).
56. N. P. van der Meulen, M. Bunka, K. A. Domnanich, C. Müller, S. Haller, C. Vermeulen, A. Türler, R. Schibli, Cyclotron production of ^{44}Sc: From bench to bedside. *Nucl. Med. Biol.* **42**, 745–751 (2015).
57. C. Müller, K. A. Domnanich, C. A. Umbricht, N. P. van der Meulen, Scandium and terbium radionuclides for radiotheranostics: Current state of development towards clinical application. *Br. J. Radiol.* **91**, 20180074 (2018).
58. C. Umbricht, M. Benešová, R. Schmid, A. Türler, R. Schibli, N. Van der Meulen, C. Müller, ^{44}Sc-PSMA-617 for radiotheragnostics in tandem with ^{177}Lu-PSMA-617—Preclinical investigations in comparison with ^{68}Ga-PSMA-11 and ^{68}Ga-PSMA-617. *EJNMMI Res.* **7**, 9 (2017).
59. J. P. Meier, H. J. Zhang, R. Freifelder, M. Bhuiyan, P. Selman, M. Mendez, P. H. A. Kankanamalage, T. Brossard, A. Pusateri, H.-M. Tsai, L. Leoni, S. Penano, K. Ghosh, B. A. Broder, E. Markiewicz, A. Renne, W. Stadler, R. Weichselbaum, J. Nolen, C.-M. Kao, S. K. Chitneni, D. A. Rotsch, R. Z. Szmulewitz, C.-T. Chen, Accelerator-based production of scandium radioisotopes for applications in prostate cancer: Toward building a pipeline for rapid development of novel theranostics. *Molecules* **28**, 6041 (2023).
60. J. Choiński, M. Łyczko, Prospects for the production of radioisotopes and radiobioconjugates for theranostics. *Bioalgorithms Medsystem* **17**, 241–257 (2021).
61. M. Sitarz, K. Szkliniarz, J. Jastrzębski, J. Choiński, A. Guertin, F. Haddad, A. Jakubowski, K. Kapinos, M. Kisieliński, A. Majkowska, E. Nigron, M. Rostampour, A. Stolarz, A. Trzcińska, R. Walczak, J. Wojtkowska, W. Zipper, A. Bilewicz, Production of Sc medical radioisotopes with proton and deuteron beams. *Appl. Radiat. Isot.* **142**, 104–112 (2018).
62. M. Pruszyński, N. S. Loktionova, D. V. Filosofov, F. Rösch, Post-elution processing of ^{44}Ti/^{44}Sc generator-derived ^{44}Sc for clinical application. *Appl. Radiat. Isot.* **68**, 1636–1641 (2010).
63. J. Qi, B. Huang, Positronium lifetime image reconstruction for TOF PET. *IEEE Trans. Med. Imaging* **41**, 2848–2855 (2022).
64. B. Huang, T. Li, G. Ariño-Estrada, K. Dulski, R. Y. Shopa, P. Moskal, E. Stępień, J. Qi, SPLIT: Statistical positronium lifetime image reconstruction via time-thresholding. *IEEE Trans. Med. Imaging* , 2148–2158 (2024).
65. H.-H. Huang, Z. Zhu, S. Booppasiri, Z. Chen, S. Pang, C.-M. Kao, A statistical reconstruction algorithm for positronium lifetime imaging using time-of-flight positron emission tomography. arXiv:2206.06463 [physics.med-ph] (2022).
66. R. Shopa, K. Dulski, Multi-photon time-of-flight MLEM application for the positronium imaging in J-PET. *Bioalgorithms Medsystem* **18**, 135–143 (2022).
67. K. Shibuya, H. Saito, H. Tashima, T. Yamaya, Using inverse Laplace transform in positronium lifetime imaging. *Phys. Med. Biol.* **67**, 025009 (2022).
68. J. Jegal, D. Jeong, E. Seo, H. Park, H. Kim, Convolutional neural network-based reconstruction for positronium annihilation localization. *Sci. Rep.* **12**, 8531 (2022).
69. A. V. Avachat, A. G. Leja, K. H. Mahmoud, M. A. Anastasio, M. Sivaguru, A. D. Fulvio, Positron annihilation lifetime spectroscopy of adipose, hepatic, and muscle tissues. [Preprint] (2022). https://doi.org/10.21203/rs.3.rs-1657111/v1.
70. G. Liu, H. Chen, L. Chakka, J. Gadzia, Y. Jean, Applications of positron annihilation to dermatology and skin cancer. *Phys. Status Solidi C* **4**, 3912–3915 (2007).
71. R. Pietrzak, S. Borbulak, R. Szatanik, Influence of neoplastic therapy on the investigated blood using positron annihilation lifetime spectroscopy. *Nukleonika* **58**, 199–202 (2013).
72. P. Vaupel, A. Flood, H. Swartz, Oxygenation status of malignant tumors vs. normal tissues: Critical evaluation and updated data source based on direct measurements with pO_2 microsensors. *Appl. Magn. Reson.* **52**, 1451 (2021).
73. D. N. Louis, A. Perry, P. Wesseling, D. J. Brat, I. A. Cree, D. Figarella-Branger, C. Hawkins, H. K. Ng, S. M. Pfister, G. Reifenberger, R. Soffietti, A. von Deimling, D. W. Ellison, The 2021 WHO classification of tumors of the central nervous system: A summary. *Neuro Oncol.* **23**, 1231–1251 (2021).
74. L. Krolicki, F. Bruchertseifer, J. Kunikowska, H. Koziara, B. Królicki, M. Jakuciński, D. Pawlak, C. Apostolidis, S. Mirzadeh, R. Rola, A. Merlo, A. Morgenstern, Prolonged survival in secondary glioblastoma following local injection of targeted alpha therapy with ^{213}Bi-substance P analogue. *Eur. J. Nucl. Med. Mol. Imaging* **45**, 1636–1644 (2018).
75. H. Alva-Sánchez, C. Quintana-Bautista, A. Martínez-Dávalos, M. A. Ávila-Rodríguez, M. Rodríguez-Villafuerte, Positron range in tissue-equivalent materials: Experimental microPET studies. *Phys. Med. Biol.* **61**, 6307–6321 (2016).
76. D. Bailey, D. Townsend, P. Valk, M. Maisey, *Positron Emission Tomography: Basic Sciences* (Springer, ed. 1, 2005), p. 22.

77. J. Cal-Gonzalez, J. L. Herraiz, S. España, P. M. G. Corzo, J. J. Vaquero, M. Desco, J. M. Udias, Positron range estimations with PeneloPET. *Phys. Med. Biol.* **58**, 5127–5152 (2013).
78. M. Bunka, C. Müller, C. Vermeulen, S. Haller, A. Türler, R. Schibli, N. P. van der Meulen, Imaging quality of ^{44}Sc in comparison with five other PET radionuclides using Derenzo phantoms and preclinical PET. *Appl. Radiat. Isot.* **110**, 129–133 (2016).
79. S. Niedźwiecki, P. Białas, C. Curceanu, E. Czerwiński, K. Dulski, A. Gajos, B. Głowacz, M. Gorgol, B. C. Hiesmayr, B. Jasińska, Ł. Kapłon, D. Kisielewska-Kamińska, G. Korcyl, P. Kowalski, T. Kozik, N. Krawczyk, W. Krzemień, E. Kubicz, M. Mohammed, M. Pawlik-Niedźwiecka, M. Pałka, L. Raczyński, Z. Rudy, N. G. Sharma, S. Sharma, R. Y. Shopa, M. Silarski, M. Skurzok, A. Wieczorek, W. Wiślicki, B. Zgardzińska, M. Zieliński, P. Moskal, J-PET: A new technology for the whole-body PET imaging. *Acta Phys. Polon. B* **48**, 1567 (2017).
80. K. Dulski, M. Silarski, P. Moskal, A method for time calibration of PET systems using fixed beta+ radioactive source. *Acta Phys. Polon. B* **51**, 195 (2020).
81. S. Sharma, J. Chhokar, C. Curceanu, E. Czerwiński, M. Dadgar, K. Dulski, J. Gajewski, A. Gajos, M. Gorgol, N. Gupta-Sharma, R. del Grande, B. C. Hiesmayr, B. Jasińska, K. Kacprzak, Ł. Kapłon, H. Karimi, D. Kisielewska, K. Klimaszewski, G. Korcyl, P. Kowalski, T. Kozik, N. Krawczyk, W. Krzemień, E. Kubicz, M. Mohammed, S. Niedzwiecki, M. Pałka, M. Pawlik-Niedźwiecka, L. Raczyński, J. Raj, A. Ruciński, S. Shivani, R.-Y. Shopa, M. Silarski, M. Skurzok, E. Ł. Stępień, W. Wiślicki, B. Zgardzińska, P. Moskal, Estimating relationship between the time over threshold and energy loss by photons in plastic scintillators used in the J-PET scanner. *EJNMMI Phys.* **7**, 39 (2020).
82. D. Sarrut, M. Bała, M. Bardiès, J. Bert, M. Chauvin, K. Chatzipapas, M. Dupont, A. Etxebeste, L. M Fanchon, S. Jan, G. Kayal, A. S Kirov, P. Kowalski, W. Krzemien, J. Labour, M. Lenz, G. Loudos, B. Mehadji, L. Ménard, C. Morel, P. Papadimitroulas, M. Rafecas, J. Salvadori, D. Seiter, M. Stockhoff, E. Testa, C. Trigila, U. Pietrzyk, S. Vandenberghe, M. A. Verdier, D. Visvikis, K. Ziemons, M. Zvolský, E. Roncali, Advanced Monte Carlo simulations of emission tomography imaging systems with GATE. *Phys. Med. Biol.* **66**, 10TR03 (2021).
83. J. Allison, K. Amako, J. Apostolakis, P. Arce, M. Asai, T. Aso, E. Bagli, A. Bagulya, S. Banerjee, G. Barrand, B. R. Beck, A. G. Bogdanov, D. Brandt, J. M. C. Brown, H. Burkhardt, P. Canal, D. Cano-Ott, S. Chauvie, K. Cho, G. A. P. Cirrone, G. Cooperman, M. A. Cortés-Giraldo, G. Cosmo, G. Cuttone, G. Depaola, L. Desorgher, X. Dong, A. Dotti, V. D. Elvira, G. Folger, Z. Francis, A. Galoyan, L. Garnier, M. Gayer, K. L. Genser, V. M. Grichine, S. Guatelli, P. Guèye, P. Gumplinger, A. S. Howard, I. Hřivnáčová, S. Hwang, S. Incerti, A. Ivanchenko, V. N. Ivanchenko, F. W. Jones, S. Y. Jun, P. Kaitaniemi, N. Karakatsanis, M. Karamitros, M. Kelsey, A. Kimura, T. Koi, H. Kurashige, A. Lechner, S. B. Lee, F. Longo, M. Maire, D. Mancusi, A. Mantero, E. Mendoza, B. Morgan, K. Murakami, T. Nikitina, L. Pandola, P. Paprocki, J. Perl, I. Petrović, M. G. Pia, W. Pokorski, J. M. Quesada, M. Raine, M. A. Reis, A. Ribon, A. Ristić Fira, F. Romano, G. Russo, G. Santin, T. Sasaki, D. Sawkey, J. I. Shin, I. I. Strakovsky, A. Taborda, S. Tanaka, B. Tomé, T. Toshito, H. N. Tran, P. R. Truscott, L. Urban, V. Uzhinsky, J. M. Verbeke, M. Verderi, B. L. Wendt, H. Wenzel, D. H. Wright, D. M. Wright, T. Yamashita, J. Yarba, H. Yoshida, Recent developments in GEANT4. *Nucl. Instrum. Methods Phys. Res. A.* **835**, 186–225 (2016).
84. P. Moskal, P. Kowalski, R. Y. Shopa, L. Raczyński, J. Baran, N. Chug, C. Curceanu, E. Czerwiński, M. Dadgar, K. Dulski, A. Gajos, B. C. Hiesmayr, K. Kacprzak, Ł. Kapłon, D. Kisielewska, K. Klimaszewski, P. Kopka, G. Korcyl, N. Krawczyk, W. Krzemień, E. Kubicz, S. Niedźwiecki, S. Parzych, J. Raj, S. Sharma, S. Shivani, E. Stępień, F. Tayefi, W. Wiślicki, Simulating NEMA characteristics of the modular total-body J-PET scanner—An economic total-body PET from plastic scintillators. *Phys. Med. Biol.* **66**, 175015 (2021).
85. M. Sitarz, J.-P. Cussonneau, T. Matulewicz, F. Haddad, Radionuclide candidates for $\beta^+\gamma$ coincidence PET: An overview. *Appl. Radiat. Isot.* **155**, 108898 (2020).

Acknowledgments: We acknowledge the strong support of E. Beyene, A. Coussat, A. Heczko, H. Giemza, P. Kapusta, P. Konieczka, S. Moyo, and P. Wasiuk. **Funding:** This work was supported by the Foundation for Polish Science through the TEAM POIR.04.04.00-00-4204/17 program (P.M.), the National Science Centre of Poland through grants MAESTRO no. 2021/42/A/ST2/00423 (P.M.) and OPUS no. 2021/43/B/ST2/02150 (P.M.), the Ministry of Education and Science through grant no. SPUB/SP/490528/2021 (P.M.), the SciMat and qLife Priority Research Areas budget under the program Excellence Initiative–Research University at the Jagiellonian University (P.M. and E.S.), and Jagiellonian University project no. CRP/0641.221.2020 (P.M.). **Author contributions:** The portable modular J-PET scanner, the positronium imaging method, and this study were conceived by P.M. P.M. and E.Ł.S. planned and supervised the research and interpreted the obtained results. The manuscript was prepared by P.M. in collaboration with E.Ł.S. and the input from J.B., K.D., A.G., G.K., D.K., K. Kubat, K. Kacprzak, S.N., S.P., S. Sharma, L. Królicki, and J.K. and was then edited and approved by all authors. Figures were conceptualized by P.M. and prepared by J.B., K.D., D.K., S.P., S. Shivani, and S. Sharma. The performed medical experiment was planned by P.M, L. Królicki, and E.Ł.S. The ethical committee consent was secured by L. Królicki and J.K. The preparation of pharmaceuticals, planning of patient examination and imaging protocols, patient preparation, imaging, and therapy management were done by L. Królicki, J.K., K.F., M. Kobylecka, and J.M. The imaging was conducted using the dedicated modular and portable J-PET apparatus developed by the J-PET collaboration. P.M., J.B., N.C., M. Das, K.D., A.G., G.K., W.K., D.K., W.Migdał, S.N., S.P., L. Królicki, and E.Ł.S. installed the J-PET scanner in the hospital, put it into operation, and carried out imaging of the patient using J-PET. Preparation of ^{44}Sc for the calibration of the detector was provided by J.C. The J-PET data analysis and calibrations were performed by K. Kacprzak, A.G., and K.D. under the supervision of P.M. Biograph PET/CT images were processed by J.B. Positronium lifetime images and their merging with CT and PET images were conceptualized by P.M. and performed by K.D. and J.B. under the supervision of P.M. Signal selection criteria were developed by P.M. P.M., J.B., N.C., C.C., E.C., M. Dadgar, M. Das, K.D., K.E., A.G., K. Kacprzak., M. Kajetanowicz, T. Kaplanoglu, Ł. Kapłon, G.K., T. Kozik, W.K., K. Kubat, D.K., W. Migdał, G.M., W. Mryka, S.N., S.P., E.P.d.R., L.R., S. Sharma, S. Shivani, R.Y.S., M. Silarski, M. Skurzok, E.Ł.S., P.T., F.T., K.T.A., W.W., and E.Ł.S. participated in the construction, commissioning, and calibration of the modular J-PET scanner. S.N. and G.K. optimized the working parameters of the scanner. K.D., A.G., K. Kacprzak, and W.K. developed the J-PET analysis and simulation framework. K. Kacprzak and A.G. developed low-level signal reconstruction methods. Ł. Kapłon developed the methods and performed plastic scintillator characterization for the scanner construction. G.K. developed, programmed, synchronized, and operated the triggerless DAQ system. M. Kajetanowicz developed the front-end electronics boards for the scanner. W. Migdał assembled the J-PET detection modules and scanner mechanical constructions. K. Kacprzak and A.G. performed timing calibration of the detector. F.T. and S.N. determined National Electrical Manufacturers Association performance characteristics of the modular J-PET scanner. K. Klimaszewski, W.W., L.R., and R.Y.S. managed the computing resources for high-level analysis and simulations. E.C. developed and operated short- and long-term data archiving systems and the computer center of J-PET. K.D. developed the PALS Avalanche program for the decomposition of positron annihilation lifetime spectra. S. Sharma established the relationship between energy deposition and TOT and the dependence of detection efficiency on energy deposition. S.P. performed Monte Carlo simulations of sensitivity profiles. S.B. contributed with the theoretical support for positronium physics. P.M. and E.S managed the whole project and secured the main financing. **Competing interests:** P.M. and G.M. are inventors on a patent related to this work [patent nos. (Poland) PL 227658, (Europe) EP 3039453, and (United States) US 9,851,456], filed (Poland) 30 August 2013, (Europe) 29 August 2014, and (United States) 29 August 2014; published (Poland) 23 January 2018, (Europe) 29 April 2020, and (United States) 26 December 2017]. J.K. reports participation on a Data Safety Monitoring Board and Advisory Board from Novartis (personal fees). The other authors declare that they have no other competing interests. **Data and materials availability:** All data needed to evaluate the conclusions in the paper are present in the paper and/or the Supplementary Materials.

Submitted 17 March 2024
Accepted 9 August 2024
Published 13 September 2024
10.1126/sciadv.adp2840